Contents lists available at ScienceDirect

International Journal of Heat and Mass Transfer

Numerical investigation of nucleate boiling heat transfer on thin substrates

A. Sanna [a], C. Hutter [b], D.B.R. Kenning [a], T.G. Karayiannis [a,*], K. Sefiane [b], R.A. Nelson [c]

[a] Brunel University, School of Engineering and Design, Uxbridge UB8 3PH, UK
[b] University of Edinburgh, School of Engineering, Mayfield Road, Edinburgh EH9 3JL, UK
[c] Los Alamos National Laboratory, Los Alamos, NM 87545, USA

A B S T R A C T

The objective of this paper is to define the guidelines for the design of new boiling test sections with a large number of artificial nucleation sites during nucleate boiling for thin substrates horizontally immersed in a saturated liquid with artificial cavities located on the upper surface. The findings of numerical simulations of pool boiling heat transfer for a single bubble and for a large number of nucleation sites based on the analysis of experimental cases were analysed. Dedicated test sections were used in experiments for the study of boiling mechanisms and interactions between active sites so that the numerical models representing the physics of the problem could be improved. The hybrid nature of the code used in this study, combining the complete solution of the three-dimensional time-dependent energy equation in the solid substrate with semi-empirical models representing the physical phenomena occurring in the liquid side, in a simplified way, allows a large number of simulations in a reasonable computational time.

The present paper focuses in the first part on the capability of the model to reproduce the experimental results for various conditions, while in the second part, the results for a large number of nucleation sites are analysed. Regarding the single bubble growth, two series of simulations will be presented in this paper: the first one analyses the mechanisms of nucleate boiling on a silicon substrate immersed in the dielectric fluid FC-72. The second series studies the behaviour of bubbles on metallic substrates, platinum and titanium, in saturated water. In the last section, the effect of the position of a site during simulations of a large population of sites (of the order of 100) on the waiting time, growth time, type and occurrence of coalescence and the thermal characteristics is presented.

1. Introduction

Boiling heat transfer has always been a very interesting research field because of the high efficiency of this process in removing heat from a solid body using liquids. Several studies focussed on the understanding of the fluid–solid combinations in order to obtain the highest heat fluxes at the minimum superheat. High values of this parameter could lead to possible alteration of thermal heat transfer characteristics of the solid substrate. However, despite the fact that research has been carried on for several decades, the complete picture of the processes involved is far from complete, due in part to the non-uniformity of the conditions and characteristics of the materials during experiments (substrates and liquids as well as measuring instrumentation), to the non-linearity

of the processes and to the possible presence of hysteresis phenomena (generally related to the activation temperature for a nucleation site significantly higher than the expected or theoretical value). Due to the complexity of the research area, the studies focus on different aspects, from the formulation of predictive correlations to dedicated experiments investigating specific aspects or to the analysis of results of complex numerical simulations. The first studies focussed on the prediction of the average heat flux between the liquid and the solid substrate and the associated maximum wall superheat, as for instance in the models suggested by Rohsenow [1] or Engelberg-Foster and Greif [2] and often based on dimensionless numbers, as described in [3]. Past studies investigated also bubble growth: the analysis of the conditions necessary for the activation of a nucleation site (for instance [4,5] or [6]) and their connection to the presence of a vapour nucleus trapped in a cavity (acting as a nucleation site) that starts growing when superheat increases. When the temperature of the walls of

* Corresponding author. Tel.: +44 1895267132.
   E-mail address: tassos.karayiannis@brunel.ac.uk (T.G. Karayiannis).

Nomenclature

Latin letters

A_h, A_v	cell lateral surface areas
c_L	specific heat of liquid
f	dimensionless factor
g	gravity acceleration
h	heat transfer coefficient
HTC	heat transfer coefficient
H_{fg}	latent heat of evaporation
i, j, k	numerical identifier
k	thermal conductivity
p	pressure
q''	heat flux
q_{vol}	volumetric heat source
Q	heat contributions
r	bubble radius
S	distance
t	time
T	temperature
V	volume
x, y, z	Cartesian coordinates
x_r	radial coordinate
w_{xy}	mesh width

Greek letters

α	thermal diffusivity
γ_{vol}	volumetric thermal expansion coefficient
δ	thickness
Δp	pressure drop
Δt	time step
ΔT	superheat
Δz	thickness of the layer
μ_L	liquid viscosity
ν_L	liquid kinematic viscosity
ρ	density
σ	surface tension

φ	contact angle

Subscripts

act	activation
air	air
av	average
b	bubble
bd	bubble departure
c	contact area
$cacav$	cavity
CL	contact line
D	dome of the bubble
$decr$	decreasing
eff	effective
enh	enhancement
eq	equivalent
g	growth
H	heater substrate
i, j, k	generic site
in	initial value
L	liquid
m	mesh
max	maximum
ML	micro-layer
NC	natural convection
NS	nucleation site
S	shape of the bubble
sat	saturation
$scal$	scaled
SEN	sensor
tot	total
W	wall
V	vapour
Vol	volume
0	initial value
φ	contact angle

the cavity with the trapped nucleus starts to increase, and if enough heat flux is provided, the nucleus grows up to the border of the cavity and then expands outside it. The shape of the growing bubble is determined by the advancing mode of the triple contact line (i.e. the theoretical line that divides liquid, solid and vapour phases, as for instance in Tong et al. [7]) at the surface immediately outside the cavity border. Kenning [8] reviewed the model of Chesters [9] for the growth of bubbles out of the cavity and related it to the bubble growth speed. Three growth models were identified for it: slow confined, slow spreading and fast bubble growths. Several studies assume that the bubble grows apparently as a truncated sphere, and that its shape is connected to the apparent contact angle, i.e. the apparent angle formed between the solid substrate and the dome. For this parameter, a distinction was made depending on whether the liquid–vapour interface was moving towards the vapour/gas region (advancing contact angle) or away from it (receding), as reported in [7]. The semi-empirical models suggested for the bubble growth, focussed on the identification of dedicated correlations for the average bubble radius and bubble departure radius (e.g. described in [10–13]). Two phases for the bubble growth were generally identified, the first one dominated by inertial forces and the second by thermal phenomena. The departure of the bubble was related to the breakdown of the equilibrium between forces that keep the bubble attached to the substrate (and in particular the surface tension) and forces trying

to detach it (gravity and hydro-dynamic lift). Departure of the bubble was observed to have a strong influence on the temperature distribution over an area larger than the bubble size due to the high heat flux during the bubble growth and mostly to the wake effect on the liquid side due to the lifting of the departed bubble. The quantification of this area, often called "influence area", was also investigated, amongst the others by Han and Griffith [14] and Mikic and Rohsenow [15], concluding the influence area to have a diameter approximately double the bubble departure diameter. The influence area and superheat distribution were also related to the waiting time, i.e. the time between the departure of a bubble and the nucleation of a new one out of the same cavity. All these theoretical and empirical models can provide useful and easy to use correlations, but they are strongly limited by their dependence to the experimental conditions to which they refer. Stephan and Abdelsalam [16] and Pioro et al. [17] analysed the differences between the use of simple general correlations (generally valid for a wide range of conditions but limited by a significantly low accuracy) and more precise predictive equations (very precise but presenting the drawback of a validity limited to a narrow range of conditions). Recently, several efforts were directed on the development of sophisticated numerical codes: this was possible because of the continuously increasing computational power as well as of the more precise experimental equipment and accuracy of the results. However, the higher the level of detail introduced in

the representing mathematical models, the more complicate the phenomena appear, making part of the scientific community merely doubt the fact that a complete understanding of the physics is even possible. The solution of the three dimensional time dependant equations for both liquid and solid domains for a large number of nucleation sites independently acting is still not achievable in reasonable computational times. Different approaches have then been studied to simplify the problem, limiting the analysis to the case of bubbles growing on the upper surface of a solid substrate horizontally immersed in a saturated liquid. Initially, a model was created for a single bubble growing out of an isolated nucleation site for a substrate modelled at constant temperature [18–20]. This approach presented two main disadvantages: firstly, the condition of isolated bubble is applicable only to low or intermediate heat fluxes, so that the density of active nucleation sites and interaction phenomena are limited. Secondly, the hypothesis of constant temperature in the substrate was shown to be unrealistic [21] and on the contrary the effects of temperature differences across the substrate were shown to play an important role in the activation of the sites [22]. However, a great advantage introduced by this model was the creation and coupling of the so-called micro and macro regions, indicating respectively the areas in proximity and around the triple contact line area. The use of this solution allows a high level of detail and a finer mesh distribution in the region with high variation of the curvature of the bubble dome, supposed here to correspond to the area with the strongest evaporation (micro-region). A similar model was also adopted by the team led by Stephan, as described for instance in [24,25], improved by the elimination of the constant temperature in the substrate. The model is still not applicable to a large number of nucleation sites due to computational limitations and to the different interactions between a growing bubble and the surrounding space. Those were studied by Zhang and Shoji [26], and four types were identified: (1) interactions through the solid substrate, (2) through the liquid, (3) between the bubble and the environment and (4) between different bubbles at adjacent sites. The interaction through the substrate strongly depends on the characteristics of the substrate itself, on its thickness and thermal conductivity, and then in general on its thermal capacity, which can lead to a more or less uniform distribution of the temperature field.

The studies on site interaction relate to the limitation or enhancement of the activity of a specific nucleation site due to the presence of another active or previously active site located at close distance. These effects, often identified respectively as inhibition and seeding effects, were connected to phenomena on the liquid side and in particular to removal or deposition of a vapour nucleus on a cavity after departure of the bubble at the adjacent site [27]. A vapour nucleus, in fact, is supposed to be trapped in the cavity or scratch acting as nucleation site either during the shrinking of the neck of the bubble while departing, as shown schematically in Tong et al. [7], or by deposition after spreading and subsequent shrinking of the contact area of a bubble at an adjacent nucleation site as described before. Considering all the uncertainties to which these phenomena are subject, this brief introductive analysis shows the main difficulties that a programmer may face while creating a new numerical model. For this reason, some physical models need to be significantly simplified and others not accounted for altogether depending on the objectives of the study and according to the computational power. The hybrid approach used for the present calculations is particularly interesting due to the possibility of studying the interactions between bubbles and the temperature distribution across the substrate. The original version of the model/code was developed by Pasamehmetoglu and Nelson [28], allowing only one bubble per cell. The code was subsequently modified, as described in Golobič et al. [29,30] using the same approach but introducing a mechanism able to refine the mesh distribution

around a nucleation site every time this becomes active. The original model/code and its subsequent improved versions were acquired and modified in this study to describe the growth of bubbles from artificial sites. In order to comply with the objectives of this work, a restructuring process was done (so that the code was also suitable for parallel computing). Moreover, several aspects of the physical model were modified and improved in order to make them more similar to experimental evidence, together with a first process of verification of the numerical code. The modifications focussed on the variation of the bubble shape and the contraction of the contact area during the final stage of the bubble growth, the different heat contributions at the dome and at the base of the bubble and finally the study of interactions between bubbles growing at adjacent sites. This study will focus on the results of simulation using different substrate-liquid conditions for a single bubble. In fact, the code will be used to simulate a silicon substrate immersed in FC-72 and a metal foil in water. The numerical results are compared to experiments carried by Hutter et al. [31] and Golobič et al. [32]. The code was also used to investigate the interactions between a large number of nucleation sites (∼100), with focus on their effects on the activity of the sites, the average bubble growth time and radius and the superheat variation at the nucleation site and in the area around it.

2. Description of the physical model used in the code

The use of a hybrid code as the one adopted for the current simulations relies on input data obtained either from experiments or from theoretical models applicable for the specified conditions. If the data is not available, assumed values must be introduced and verified afterwards. The data are related to an isolated growing bubble as well as to the properties of the liquid and substrate and the numerical input used for mesh management. The most important data are listed here:

- The bubble departure radius r_{bd}, i.e. the final radius that the bubble assumes when departing.
- The growth time (when available) t_g, i.e. the time that the bubble requires to reach the bubble departure radius from nucleation.
- The apparent contact angle φ_0, i.e. the angle between the substrate and the bubble, supposed to grow as a truncated sphere. This value is not a real physical value and should not be confused with the real contact angle, which is determined by the balance of the forces acting on the bubble at each instant and which may strongly depend also on the shape of the cavity and other thermal–hydraulic factors.
- The activation conditions for a nucleation site and the average superheat of the substrate ΔT_{av}. It is assumed in the code that activation occurs when the temperature at the nucleation site exceeds a fixed value called activation temperature T_{act}.

As mentioned before, the approach is based on a mesh distribution that is modified when a nucleation site becomes active in order to have a finer mesh around it. The original version of the model used an irregular distribution of triangular cells that was locally refined around an *active* nucleation site, as shown in Fig. 1. The present model uses square cells arranged in a Cartesian grid, as shown in Fig. 2. In both cases, (a) represents the phase where no nucleation site is active and the mesh distribution is coarse; once the conditions for activation of a site (described later) are satisfied (b) the mesh located around the nucleation site in a pseudo-circular region are removed and replaced (c) by a finer mesh distribution arranged with central symmetry. The cell distribution is identically repeated for all the layers in which the
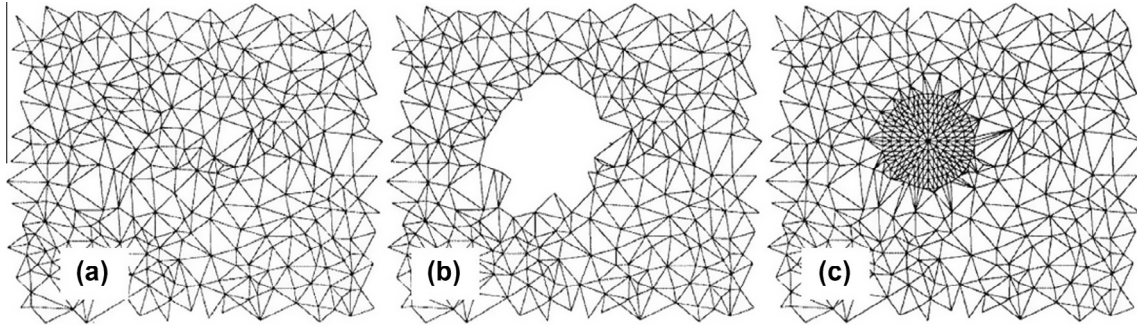
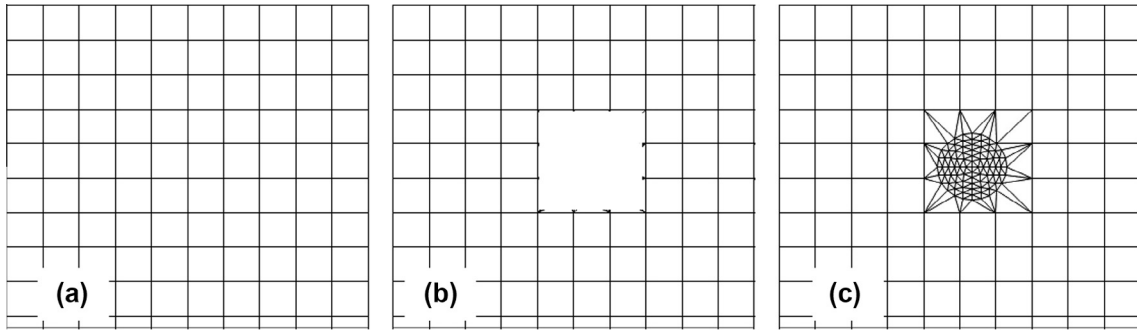**Fig. 1.** Mesh distribution for cells with triangular base – irregular distribution [30].

Fig. 2. Mesh distribution for cells with square base – regular distribution.

substrate is vertically divided, for both cases of active and inactive nucleation sites (respectively unrefined and refined mesh). This process allows fast simulations and the location of the nucleation sites in whichever position in the upper surface of the substrate.

At the beginning of the simulations, the code automatically numbers the cells with a progressive identification number. Once a nucleation site activates, the cell identification numbers are changed, and the new refined cells assume high values. For each cell, following the numbering and starting from the top layer, the code solves (with an explicit method) the 3-dimensional (x, y, z) time dependent (t) energy equation (Eq. (1)). The discretised form, shown in Eq. (2), is used in the code in order to calculate the temperature T in each cell from the contribution of the heat through the surfaces at the interface with the other cells or the boundaries. q_{vol} represents the volumetric heat source that may be present to simulate for instance electrically induced heat generation; its value can be also set equal to zero, as it was during the present simulations.

$$\frac{\partial T}{\partial t} = \frac{k_H}{\rho_H c_H}\left(\frac{\partial^2 T}{\partial x^2} + \frac{\partial^2 T}{\partial y^2} + \frac{\partial^2 T}{\partial z^2}\right) + \frac{q_{vol}}{\rho_H c_H} \tag{1}$$

$$
\begin{aligned}
Q = {}& q_{vol}A_{v,k}\Delta z + A_{v,k} \\
& \times \frac{k_H}{\Delta z}[T(\bar{t};k,z-1) - 2T(\bar{t};k,z) + T(\bar{t};k,z+1)] + \sum_j A_{h,k-j} \\
& \times \frac{k_H \Delta z}{S_{k,j}}[T(\bar{t};k,z) - T(\bar{t};j,z)]
\end{aligned} \tag{2}
$$

The symbols of the single cell variables as shown in Fig. 3.

At the initial time step $(t = 0\ \text{s})$ the temperature for all the cells and all layers is set equal to a fixed value (T_{in}), either equal to the saturation temperature or higher. The code imposes that the temperature at the lateral edges of the substrate is equal to the saturation temperature, as expressed in Eq. (3), with the symbols as in Fig. 4. For the bottom surface $(z = 0)$, natural convection with the
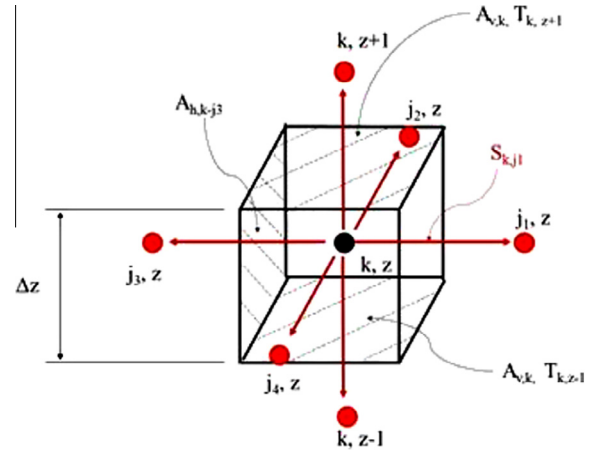

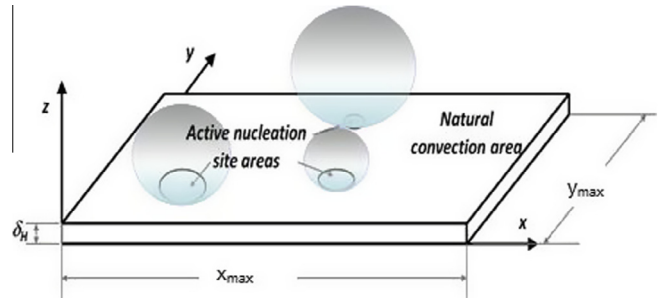**Fig. 3.** Geometry of a cell.

Fig. 4. Geometry of the substrate [30].

surrounding area is supposed, as expressed in Eq. (4), with h_{air} equal to zero if adiabatic conditions are to be simulated.

$$T|_{x=0, x=x_{\max}, y=0, y=y_{\max}; 0 \leq z \leq \delta_H} = T_{sat} \tag{3}$$

$$\left. \frac{\partial T}{\partial z}\right|_{0\leq x\leq x_{max},0\leq y\leq y_{max},z=0} = h_{air}(T - T_{air}) \tag{4}$$

For each nucleation site i, an activation temperature, $T_{act,i}$, is assigned; for each of the inactive sites, at each time step, the code checks the temperature for the cell $\bar{k}$ corresponding to its centre. If the value exceeds the activation temperature, Eq. (5), and if the not-overlapping mesh condition is satisfied (Eq. (13) discussed later), activation of the site occurs, and the mesh distribution is locally refined as described before. The bubble grows until departure, which occurs when the equivalent bubble radius $r_{eq,i}(t)$ reaches a maximum value, called bubble departure radius $r_{bd,i}$, Eq. (6), specified by the user for each nucleation site on the base of experimental or literature data.

$$T(t,\bar{k},z_{\delta_H}) \geq T_{act,i} \tag{5}$$

$$r_{eq,i}(t) \geq r_{bd,i} \tag{6}$$

The activation of a nucleation site depends on the activation superheat, ΔT_{act}, which can be imposed either as a constant or, if experimental data are not available, can be calculated from Eq. (7), supposing that the activation temperature is the minimum temperature necessary for a nucleus of radius equal to the cavity radius to start growing.

$$\begin{cases} \Delta p = 2\sigma/r_{cav} & \text{(a)} \\ \log_{10}p(Pa) = 9.729 - 1562/T(K) & \text{(b)} \end{cases} \tag{7}$$

For a cavity of fixed cavity mouth radius (r_{cav}) and surface tension (σ), the minimum overpressure (Δp) needed for the bubble to start growing is defined by Eq. 7(a). From Eq. 7(b), with values specific for FC-72 (based on [33]), the saturation temperature at experimental conditions and the temperature at a pressure equal to the experimental value plus the overpressure may be calculated. The activation superheat can then be derived. Alternative criteria may be studied and easily introduced in the code, based for instance on variations of the superheat instead of its absolute value. Moreover, a modifiable uncertainty parameter has been added to the nominal activation superheat to simulate the uncertainty of data from experimental results. At activation (occurring for instance at $t = t_0$) the bubble starts from a zero bubble radius, $r_{b,i}(t_0) = 0$, so that the initial nucleus radius is neglected. From the following time step, the bubble grows as a truncated sphere with a fixed apparent
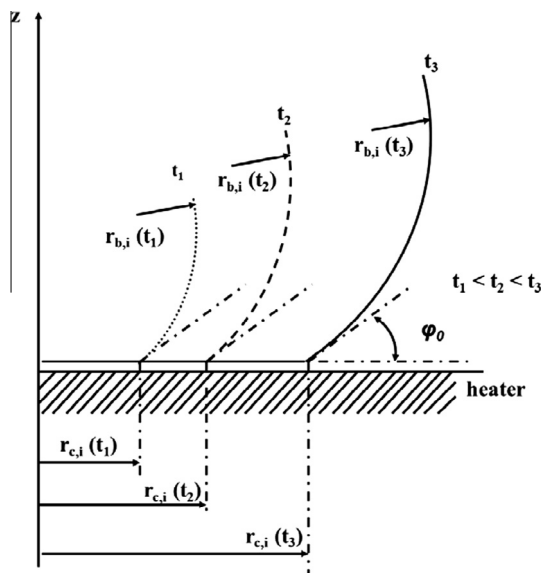

Fig. 5. Advancing triple contact line.

contact angle from nucleation to departure $\varphi = \varphi_0$. Evaporation occurs at the contact area (i.e. the region enclosed by the triple contact line) and at the dome of the bubble, as described in Eq. (8). The term on the left side represents the cumulative heat due to evaporation at the considered time step; the first term on the right side represents the cumulative heat at the previous time step; the second and third terms account for evaporation in the inner area (with heat transfer coefficient $h_{in} = HTC_{in}$) and contact line area ($h_{CL} = HTC_{CL}$). The last term $Q_{D,i}$ accounts for the evaporation at the dome. The equivalent bubble radius is calculated according to Eq. (9), assuming a truncated sphere shape for the bubble. The bubble radius $r_b(t)$ is then obtained by considering the shape of the bubble.

The contact area radius is then calculated, $r_c(t) = r_b(t)\sin\phi$. Fig. 5 shows the fundamental bubble growth parameters for the advancing triple contact line.

$$Q_{b,i}(\bar{t} + \Delta t) = Q_{b,i}(\bar{t}) + \sum_{\substack{(x_j,y_j)\in \\ inner\ area}} A_{v,j}HTC_{in,j}[T(\bar{t};j,\delta_H) - T_{sat}]\Delta t$$
$$+ \sum_{\substack{(x_j,y_j)\in \\ triple\ cont\ area}} A_{v,j}HTC_{CL,j}[T(\bar{t};j,\delta_H) - T_{sat}]\Delta t + Q_{D,i} \tag{8}$$

$$r_{eq,i}(\bar{t} + \Delta t) = \sqrt[3]{\frac{3Q_{b,i}(\bar{t} + \Delta t)}{4\pi\rho_V H_{fg}}} \tag{9}$$

Three different areas have been identified for the heat transfer coefficient imposed on the upper surface, depending whether the cell is located outside, inside or at the border (i.e. the triple contact line) of the contact area. For the region outside the bubble contact area, a natural convection heat transfer coefficient ($h_{NC} = HTC_{NC}$) is assumed, which in the specific case of a silicon substrate immersed in FC-72 [34] is given in Eqs. (10) and (11) for the case of a metal foil in water, [30].

$$h_{NC} = HTC_{NC} = f_{enh}314[T - T_{sat}]^{0.2} \tag{10}$$

$$h_{NC} = HTC_{NC} = f_{enh}0.14\rho_L c_L\left[\frac{\gamma_{vol}g}{\upsilon_L}\left(\frac{k_L}{\rho_L c_{pL}}\right)^2 (T - T_{sat})\right] \tag{11}$$

For the heat transfer model at the contact area, two models can be used in the code at the moment (although the code is very flexible and new ones may be easily implemented), as shown in Fig. 6: the micro-layer model (ML) supported by recent experimental results of [35] and the contact line model (CL) supported by Stephan and Hammer [24] and Stephan and Fuchs [36].

For the first model, a thin film of liquid (micro-layer) is supposed to be trapped between the bubble and the substrate leading to pure conduction in the liquid, so that $HTC = \frac{k_L}{\delta_{ML}}$. The heat transfer coefficient distribution presents a peak at the centre of the contact area (i.e. the micro-layer is supposed to have its minimum thickness) and a radial decrease, with no high heat transfer value near the triple contact line. The latter model assumes that a strong evaporation occurs at the triple contact line while a zero heat transfer coefficient is supposed in the inner area. The contact line model CL imposes a very high heat transfer coefficient in the triple contact line area, corresponding to the circular perimeter of the contact area of radius $r_c(t) = r_b(t)\sin\varphi$. In this area, pure conduction in the liquid micro-layer of thickness δ_{ML} occurs, as shown in Eq. (12). The thickness of the micro-layer is also defined as input data by the user at the beginning of simulations, so that the heat transfer coefficient in this area is indirectly imposed. The width of the contact line area corresponds to the width of the refined cells in the radial direction (dependent on the bubble size at departure and number of rings used for the refined mesh area). It is generally much larger than the theoretical contact line area, so that the heat
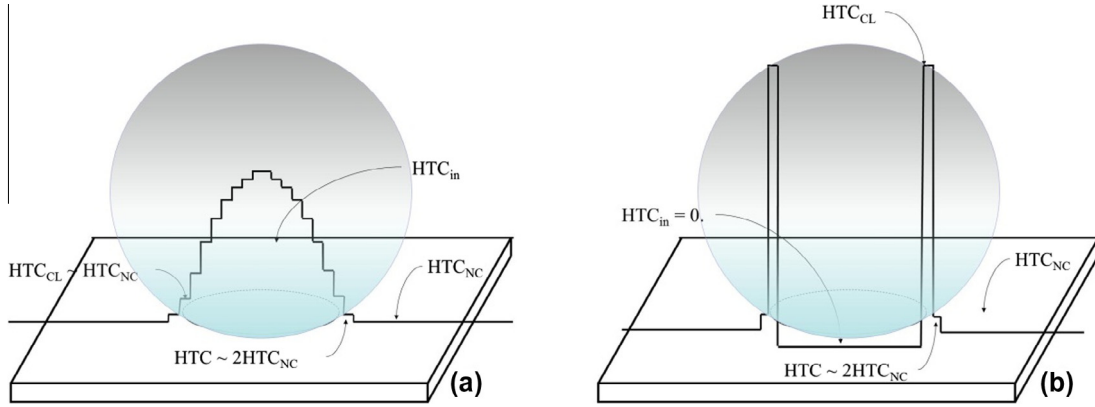
Fig. 6. Heat transfer coefficients models: (a) Micro-layer model (*ML*); (b) Contact Line model (*CL*).

transfer coefficient values are required to be scaled to obtain the correct heat flux from the area.

$$h_{CL} = HTC_{CL} = \frac{k_L}{\delta_{ML}} \tag{12}$$

It is not clear which of the two models is to be chosen and when to be applied. Different studies support one or the other model (as in [35,24,36]) and for this reason it was here opted to have a flexible model able to simulate both.

The second contribution to the bubble growth is due to the evaporation at the dome. This has been seen to be very important in determining the bubble growth rate and also to provide a significant contribution with increasing final size of the bubble. For this reason a simple evaporation model has been implemented based on Eq. (13): $Q_{D,i}$ represents for site i the cumulative heat contribution through the dome of the bubble from the activation time $t_{act,i}$ to the generic instant t when the bubble has an effective radius $r_{b,i}(t)$; $f_{D,i}$ is a constant parameter, generally equal either to 0 or 1 (but it in principle may assume whichever positive value) to adjust the evaporation contribution at the dome; $f_{S,i}(t)$ is a time-dependant geometrical shape factor introduced to take into account the truncated sphere shape. $T_{eff,i}$ in Eq. (14), depends on the activation temperature defined for each site; it is defined by assuming that the external part of the liquid thermal layer around the bubble dome stays at a temperature equal to the activation temperature $T_{act,i}$ throughout the whole bubble growth.

$$Q_{D,i} = f_D \left[4\pi . r_{b,i}^2 f_{S,i}(t) \right] \cdot \left[k_l \frac{(T_{eff,i} - T_{sat})}{\sqrt{\pi \alpha_L (t - t_{act,i})}} \right] \Delta t \tag{13}$$

$$T_{eff,i} = \frac{T_{act,i} + T_{sat}}{2} \tag{14}$$

The effect of this contribution is particularly relevant for large bubbles or for very thin or poorly conductive substrates, as shown in the next sections during the analysis of the numerical results.

Once the site becomes active, the bubble is assumed to grow as a truncated sphere with a constant apparent contact angle during the first stage of the bubble growth, and decreasing to zero with the inverse of the volume of the bubble when the bubble radius exceeds a fixed fraction of its maximum value, according to Eq. (15).

$$\varphi_i(t - t_{act}) = \begin{cases} \varphi_0 & \text{if } r_{b,i}(t - t_{act}) < f_{\varphi,decr} r_{bd,i} \\ \varphi_0 \frac{1}{1 - f_{\varphi,decr}^3} \left[1 - \frac{r_{b,i}^3(t - t_{act})}{r_{b,i}^3} \right] & \text{if } r_{b,i}(t - t_{act}) > f_{\varphi,decr} r_{bd,i} \end{cases} \tag{15}$$

This method, which allows an increasing and then decreasing contact area with consequent advancing and receding contact line, was introduced also to limit the problems of bubble at adjacent nucleation sites growing at alternative times, mentioned before. In fact, the code does not allow the presence of overlapping mesh due to two (or more) close refined sites. Two sites cannot be active at the same time if their distance S does not satisfy Eq. (15).

$$S > 1.2(r_{m,i} + r_{m,j}) + 1.0w_{xy} \tag{16}$$

This limitation may lead in some cases to nucleation sites that alternate in activation, due to numerical reasons and this effect must be taken into account while analysing the results. The replaced area has a radius r_m slightly larger than the maximum contact area $r_{c,max}$ (reached, in the original version of the code, at bubble departure since the apparent contact angle has a fixed value, so that $r_{c,max} = r_{bd} \cdot \sin(\varphi_0)$; in the new version of the code, the maximum contact area is reached sometimes before departure and its value is smaller than in the original version, due to the shrinking of the contact area during the final phase of the bubble growth); its value may vary from site to site. When the site becomes inactive again, the original coarse cell distribution is restored. All the variables are indicated in Fig. 7.

Coalescence phenomena, not taken into account in the original version of the code, are considered to have a very important impact on heat transfer rates. Three kinds of coalescence may be identified in literature: horizontal, declining and vertical coalescence. According to the conclusion of Shoji et al. [23], vertical coalescence does not depend on the distance between nucleation sites and on site population. This phenomenon is not taken into account in the code yet. On the other hand, horizontal coalescence is considered to have a very large influence on the heat transfer rates between the substrate and the liquid and to possibly induce significant temperature variations. For this reason, a very simplified model for horizontal coalescence has been introduced for two or more bubbles growing in close proximity so that their domes may come in contact while the contact areas are still separated (so that the limitation on mesh distribution as expressed in Eq. (16) is satisfied). At the moment, the model supposes the occurrence of coalescence once the bubble domes come in contact. Two situations, both of them observed in Golobič et al. [32], are considered at present, as shown in Fig. 8:

(a) Coalescence type C1: If the bubbles have similar sizes, they are assumed to continue growing as two independent isolated bubbles (with truncated sphere shape), with interfering domes, but with no variations of the heat transfer coefficients between the substrate and the liquid. Deformation of the bubble is not taken into account. The bubbles
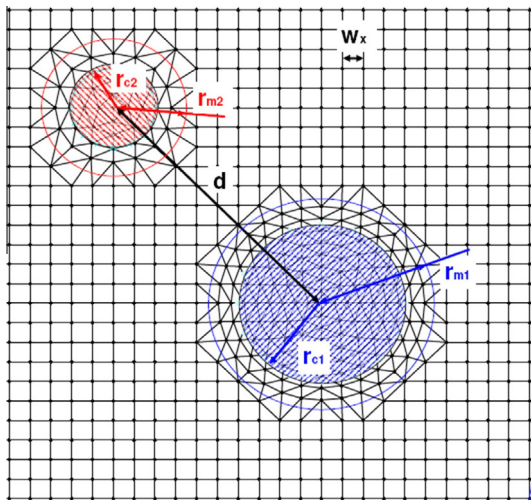
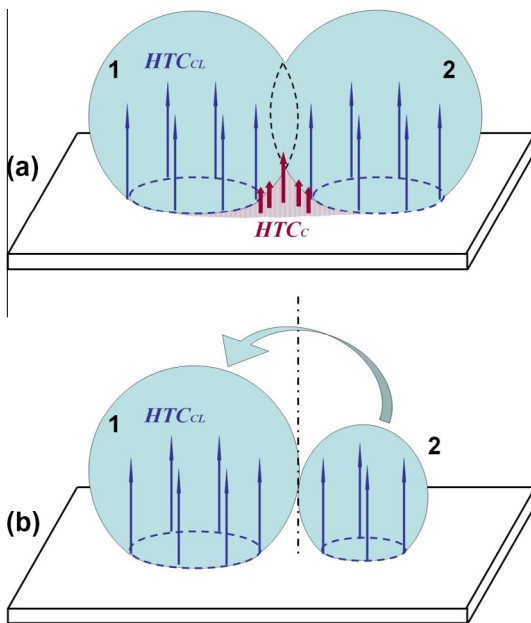**Fig. 7.** Minimum distance between active sites.

Fig. 8. Coalescence models.

grow independently until each of them departs when the defined bubble departure radius is reached. An improvement to this model may be implemented by introducing an enhancing heat transfer coefficient (HTC_C) in the area below the interfering domes: this would take into account the strong evaporation in the new contact area of the elongated shape of the bubble. Several bubbles may coalesce at the same time.

(b) Coalesce type C2: If the sizes of two bubbles are significantly different (at present, if the bubble radii ratio is equal or larger than 2.0) the smaller bubble (2) is assumed to be instantaneously absorbed by the larger bubble (1), and then completely disappear. Bubble (1) undergoes a sudden increase in volume equal to the volume of bubble (2). The bubble departure radius is then increased according by a factor accounting for the inclusion of the smaller bubble volume into the bigger bubble. The bubble departure diameter is also modified in order to avoid the possibility for the bigger bubble to disappear immediately after inclusion by exceeding its

maximum bubble size. Moreover, this solution allows simulation of multiple sequential coalescence, as may happen when a large bubble absorbs several smaller bubbles one after the other. A further improvement may be included in this model, by assuming a fast detachment phase of the small bubble after coalescence instead of instantaneous inclusion and disappearance.

The model does not consider coalescence between an attached bubble and a detached bubble from adjacent sites (declining coalescence), so that a review would be necessary if this type of coalescence was found to have a strong influence.

3. Numerical and experimental results

Two series of simulations have been run to reproduce the experimental behaviour of a bubble growing out of an isolated nucleation site. The first series refers to experiments carried out by Hutter et al. [31] for a silicon substrate (380 μm thick) completely immersed in dielectric FC-72 at saturation conditions. The details of the experimental facility and results can be found in [31]. The second series of simulations refers to the experimental results described in Golobič et al. [32,35], respectively for titanium (25 μm thick) and platinum (7 μm thick) foils immersed in water at atmospheric pressure and saturated conditions. In both cases, the main experimental results will be only summarised here, while the study will focus on the analysis of the numerical results for the bubble activity, superheat variations during the bubble growth at the nucleation site and in the area around it.

4. Single bubble growth: silicon substrate on FC-72

The experimental results refer to five bubble growth cases (each of them obtained as average value of several bubble growths at specified experimental conditions) for bubble growing out of an isolated nucleation site, but referring to imposed heat fluxes applied to the back of the substrates, ranging from 0.46 to 13.4 kW/m², as summarised in Table 1 together with the measured average wall superheat (ΔT_W), the average bubble departure radius (r_{bd}) and the bubble growth time (t_g), see [31]. Three different test sections were used as substrates during the experiments. Test section #1, a circular disc of radius equal to 762 mm and thickness 0.38 mm, was only used to test the rig. Test section #2 was 19×39.5 mm², with a heated area of 15×10 mm² with artificial cavities 10 μm in diameter 40, 80 and 100 μm deep (although the results were taken only from the 100 μm deep cavity), with temperature sensors located on the back of the substrate. For test section #3, the cavity of interest was 10 μm in diameter and 80 μm deep, with temperature sensors located around the nucleation site on the upper surface of the substrate. The contact line heat transfer model was imposed for these simulations, with a high heat transfer in the contact line region and a zero heat flux in the inner part of the contact area. The bubble growth histories are shown in Figs. 9–13 with comparison with the results from simulations. Coalescence was never observed during these experiments.

Table 1
Summary of experimental results (Hutter et al. [31]).

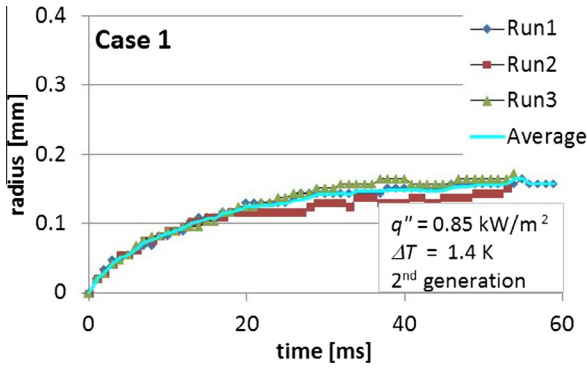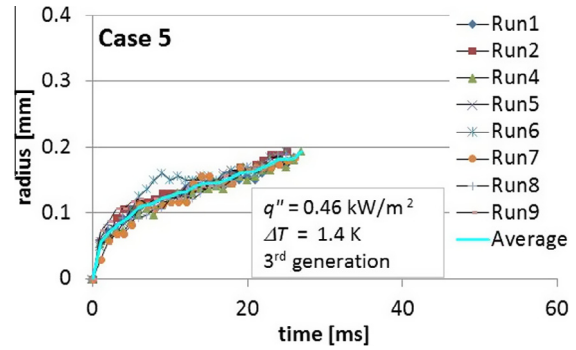| Case	Test section	q'' [kW/m²]	ΔT_W [K]	f_{enh} [–]	r_{bd} [mm]	t_g [ms]
1	2nd	0.85	1.4	1.97	0.16	59.0
2	2nd	13.4	10.1	2.66	0.36	24.0
3	3rd	4.48	8.1	1.16	0.33	21.0
4	3rd	2.36	4.8	1.14	0.22	18.0
5	3rd	0.46	1.4	0.98	0.19	27.0

Fig. 9. Experimental bubble growth showing bubble growth radius versus time for case 1 ($q'' = 0.85$ kW/m^2).

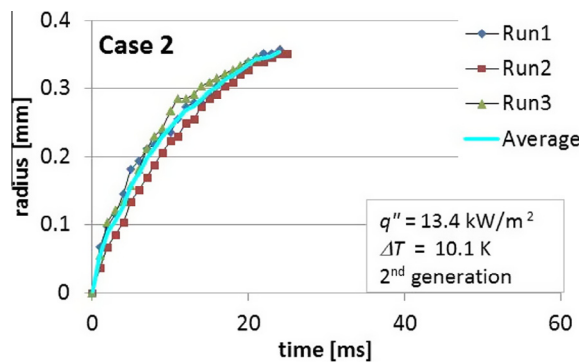**Fig. 10.** Experimental bubble growth showing bubble growth radius versus time for case 2 ($q'' = 13.4$ kW/m^2).

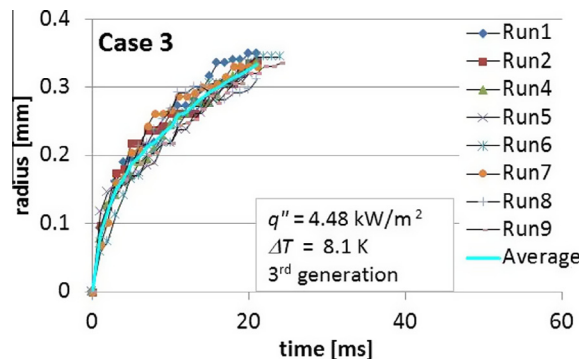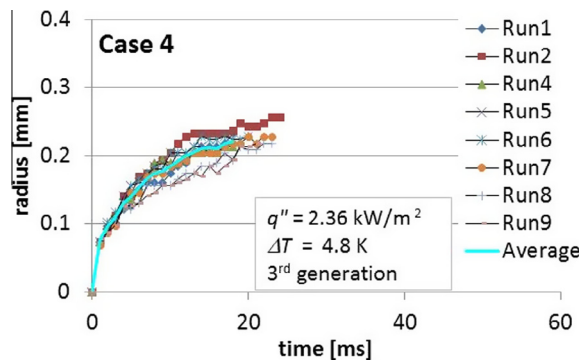**Fig. 11.** Experimental bubble growth showing bubble growth radius versus time for case 3 ($q'' = 4.48$ kW/m^2).

Fig. 12. Experimental bubble growth showing bubble growth radius versus time for case 4 ($q'' = 2.36$ kW/m^2).

Fig. 13. Experimental bubble growth showing bubble growth radius versus time for case 5 ($q'' = 0.46$ kW/m^2).

Figs. 9–13 show that the experimentally measured bubble radius varies strongly with the applied heat flux, but it does not significantly change once the heat flux is fixed. A direct correlation between the variation of the heat flux and the variation of the bubble radius was not observed. For an applied heat flux of 0.46–13.6 kW/m^2, the bubble radius varied from 0.16 to 0.35 mm (more than double) with growth times even more unpredictable, ranging from 59 to 24 ms, with a minimum of 18 ms for $q'' = 2.36$ kW/m^2. The comparisons between the experimental and simulated dimensionless bubble growth for the five cases under the two conditions of $f_{decr} = 0.6$ and 0.9 are shown in Fig. 14 respectively (a) and (b). The natural convection enhancement factor f_{enh}, was modified for each simulation to match the experimental superheat. In the figure, the time has been made dimensionless by dividing it by the average growth time (t/t_g), while the dimensionless bubble radius has been obtained by dividing the bubble radius by the bubble departure radius (r_b/r_{bd}). The figure shows that the code is able
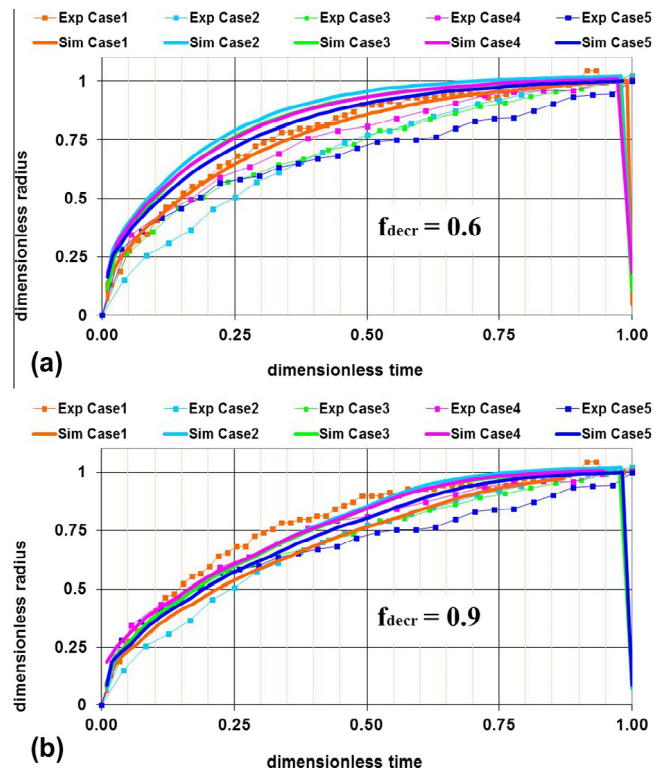

Fig. 14. Comparison of experimental and simulated dimensionless bubble growths. (a) $f_{decr} = 0.6$; (b) $f_{decr} = 0.9$.

to reproduce well the bubble growth histories under different conditions and that all the bubbles grow similarly if the dimensionless values are considered. The parameters used here to reproduce the single bubble growth will be used, unchanged to study the interactions between nucleation sites. The analysis of long term bubble growth histories showed that significantly long inactivity times have been detected for the cases with applied low heat fluxes (and consequently low wall superheat), cases #1 and #5, but the physical reason of this phenomenon is still unknown. The code is then unable to reproduce it, due to the fact that during the simulations the superheat at the top surface was always higher than the activation superheat. This could suggest that the condition use for activation (based only on the punctual superheat values) could be too restrictive. The inactivity time may in fact depend on local hydro-dynamic effects in the liquid side, as for instance agitation and wake effects after the departure of the bubble.

For case #3 (where an applied heat flux of 4.48 kW/m² was used), a more detailed analysis has been carried out, as shown in Fig. 15: a good agreement for the superheat variation (ΔT_{SEN}) for an area corresponding to the experimental size of the sensors (0.84×0.84 mm²) can also be seen. However, the variation is very small for both experiments and simulations (<±0.2 K) and significantly lower than the sensitivity of the sensors themselves, so that a proper agreement or disagreement cannot be deducted from the comparison. For larger bubble departure radii, the superheat variations are expected to be larger. However, large variations randomly distributed, as seen in experiments, are probably due to the uncertainties in measurements and not directly related to the bubble growth. In simulations, if the degree of superheat is larger than the activation superheat, the nucleation site may appear continuously active, with negligible waiting time. Fig. 15 highlight that for a faster departure process (higher f_{decr}), the bubble growth is more linear, reducing the effect of fast growth during the initial phase and slow towards the end. A similar effect can be observed in simulations varying the heat contribution at the dome of the bubble. The higher the contribution, the more linear the bubble growth becomes. For this case, the superheat variation along a line passing through the nucleation site at the beginning (3 ms) and
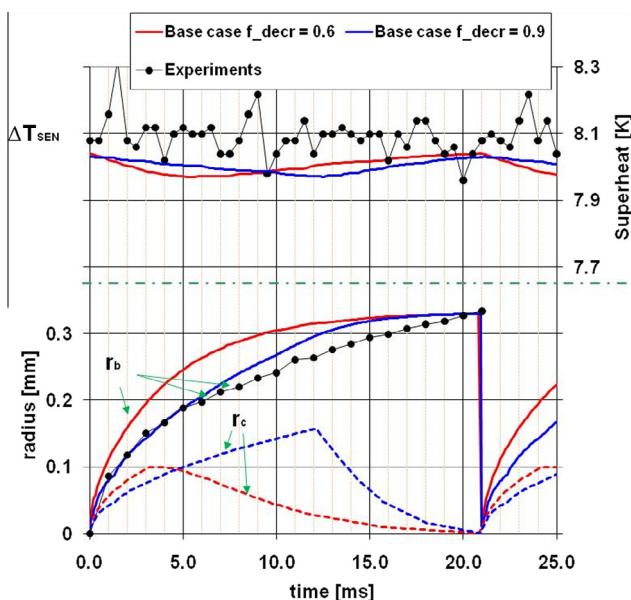
end (20 ms) of the bubble growth is shown in Fig. 16, on the top and bottom surfaces of the substrate, as well as the comparison of the growing bubble (supposed a truncated sphere) with the sensor size. It can be noted that the attenuation effect due to the thickness of the substrate (380 μm), that tends to level all local variations, similarly to what happens when measuring with a sensor of the same size of the bubble, is clear in the figure. From the analysis of the variation on the top substrate, two different distributions can be seen at the two different time steps. For $t = 3$ ms, two large negative peaks are located around the contact line, with values significantly lower than in the area far from the nucleation site (for instance for $x \sim 8$ mm, i.e. at ~1 mm from the nucleation site that is located at $x = 9$ mm). Moreover, a partial superheat recovery can be observed at the nucleation site, due to the zero heat transfer coefficient in the inner part of the contact area. Also in this case, the maximum simulated superheat variation is ~0.4 K, smaller than the sensitivity of the sensors (±0.5 K, [31]). From the analysis of the second time sequence ($t = 20$ ms), only one central negative peak can be identified, due to the fact that the contact area has already contracted so that only one mesh cell is involved, with a superheat variation significantly smaller than at the previous time steps (the shrinking of the contact area reduces the area of large HTC).

5. Single bubble growth on thin metal substrate in water

The second comparison for the single bubble growth was developed for experiments on thin metal foils immersed in saturated water. The micro-layer heat transfer mode was imposed for these simulations, with a high heat transfer at the centre of the contact area. The maximum value of the heat transfer to be used in the model is obtained from experimental results and it depends on the liquid-foil combination. Two series of experiments were used, both developed by Golobič et al. [32,35], using either a titanium foil 25 μm thick with an applied heat flux of 50 kW/m² or a platinum foil 7 μm thick with an applied heat flux of 100 kW/m², respectively. From the analysis of the dimensionless heat transfer coefficient at the nucleation site (scaled by the maximum value as obtained from experimental data, and equal to 54 kW/m²K for the titanium experiments and to 105 kW/m²K for the platinum experiments) versus the dimensionless time (scaled by the bubble growth time) a very important resemblance for the two cases has been observed here for the first time by the present authors.
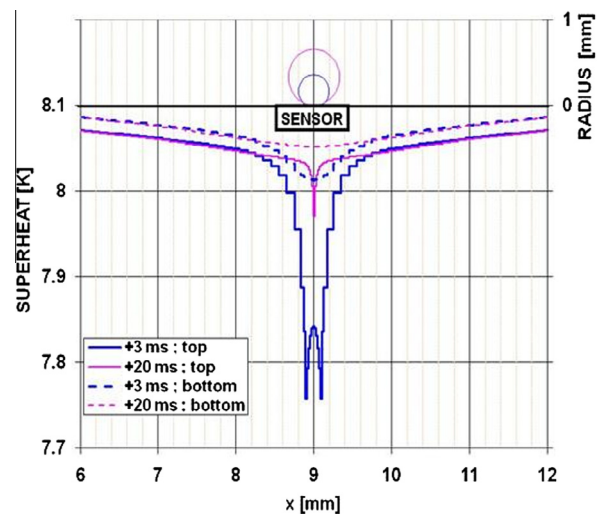

Fig. 15. Comparison of experimental and simulated dimensionless bubble growths. (a) $f_{decr} = 0.6$; (b) $f_{decr} = 0.9$, case 1 ($q'' = 4.4$ kW/m² with a measured superheat of 8.1 K, corresponding to an average bubble growth radius and time of 0.33 mm and 21 μs respectively).

Fig. 16. Bubble dimension and superheat distribution along a diametric line, for case 1 ($q'' = 4.4$ kW/m² with a measured superheat of 8.1 K, corresponding to an average bubble growth radius and time of 0.33 mm and 21 μs respectively).

Results are shown in Fig. 17. Although the values have been directly taken from the studies with no further manipulation, the results appear surprisingly similar. For this reason, the heat transfer coefficient distribution with time has been imposed in these simulations for these two cases, in difference to the previous case, where the HTC was obtained from tuning on the bubble growth time. The maximum HTC_{max} values, together with the growth time t_g and the bubble departure radius r_{bd} as listed in Table 2, were used as input data. It must be noted that the characteristics of the substrate may be affected by uncertainties due to their dependence on their exact composition, leading to a possible over-estimate of the input heat flux, Kenning et al. [37].

The tuning effect during these simulations was applied to the heat contribution at the dome, varied in order to match the experimental growth time. This contribution was seen to be very important in both the cases with metal foils, contrary to the case of the silicon wafer in water, where it was negligible. This is probably related to the bubble size, much larger in the metal foil case, so that the bubble dome surface (to which the dome contribution is proportional) is larger.

With regards to the case of the titanium foil, the values explicitly provided in Golobič et al. [10] for the bubble growth are only the time when the bubble reaches its maximum contact area radius ($t = 6$ ms) and the departure time ($t = 18$ ms). The other data used here to compare the simulations with the experimental results are listed in Table 3. The contact area radii (r_c) and the superheat at the nucleation site (ΔT_{NS}) at different time steps were derived from analysis of the temperature distribution along a line
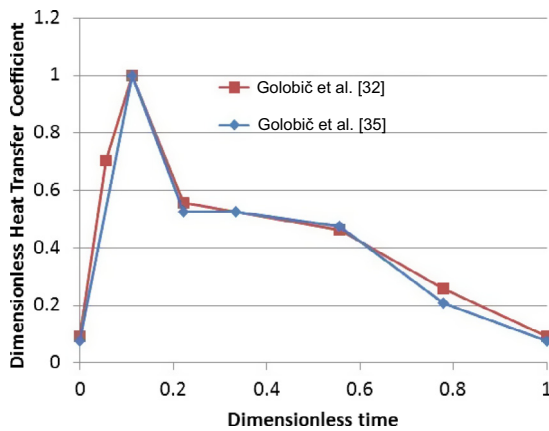
shown in [32]. On the other hand, the bubble radius values (r_b) were obtained from the analysis of the bubble growth sequence. In both cases, the data may be affected by uncertainties, which are difficult to estimate, due to the quality of the figures in [32] and resolution when reading them. Also the apparent contact angle (equal to 45°) has been chosen from analysis of the bubble growth sequence, although its value is only a rough approximation due to the mirror effect. The value for the activation superheat (15.5 K) was chosen according to the analysis described in [30] for a stainless steel substrate immersed in saturated water; a value that agreed to that shown in the experimental results of [35]. Similarly, the natural convection heat transfer coefficient was maintained, with an enhancing factor able to guarantee a superheat of ~17 K in the region outside the contact area in order to agree with the experimental results presented in [32]. The micro-layer heat transfer coefficient model has been applied to the inner part of the contact area. Its maximum value has been obtained from observation of the experimental data.

Fig. 18 shows a very good agreement between numerical and experimental results for bubble radius, superheat and heat transfer coefficient histories at the nucleation site. This shows that the model is a reasonably good representation of the physics and the code is able to reproduce the growth of a single bubble provided the correct heat transfer coefficients are applied. However, it appears that simulations slightly underestimate the bubble radius and contact area radius. A visual comparison of the bubble size at the steps of Fig. 18 is shown in Fig. 19. It must also be pointed out that the experimental results may be affected by uncertainties and optical effects.

Fig. 20 shows the superheat distribution along a line passing through the nucleation site at different time steps from simulations (on the right side) in order to compare with the experimental results (left side) from [32], together with the contact area diameter (on the top of the graph). The area outside the contact area influenced by the bubble in simulations appears to be slightly smaller than for experiments. Also, the small peaks in superheat that can be observed immediately outside it ($x \sim 18.4$ mm) for instance at $t = 0, 1, 2$ ms, which are probably due to hydro-dynamic
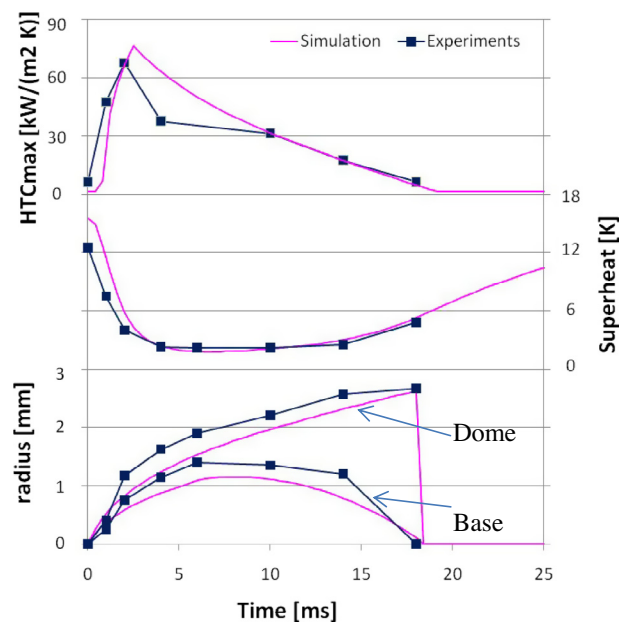

Fig. 17. Dimensionless heat transfer coefficient ($HTC(t)/HTC_{max}$) versus dimensionless time (t/t_g).

Table 2
Bubble growth characteristics.

Substrate	r_{bd}	t_g	HTC_{max}
Titanium	2.67 mm	18 ms	54 kW/m² K
Platinum	1.1 mm	9 ms	105 kW/m² K

Table 3
Bubble growth data and superheat values at the nucleation site (Golobič et al. [32]). The data were obtained from figures in the papers and are hence subject to a degree of uncertainty.

t [ms]	0	1	2	4	6	10	14	18
r_b [mm]	0	0.40	1.17	1.63	1.90	2.17	2.44	2.67
r_c [mm]	0	0.26	0.76	1.14	1.40	1.34	0.60	0
ΔT_{NS} [K]	12.5	7.5	4.0	2.3	2.2	2.2	2.5	4.8
HTC_{max} [kW/m²]	5	38	54	30	NA	25	14	5

Fig. 18. Comparison between experimental [32] for a 25 μm thick titanium foil with applied heat flux of 50 kW/m² and simulation results for bubble and contact radii, superheat and HTC_{max}.
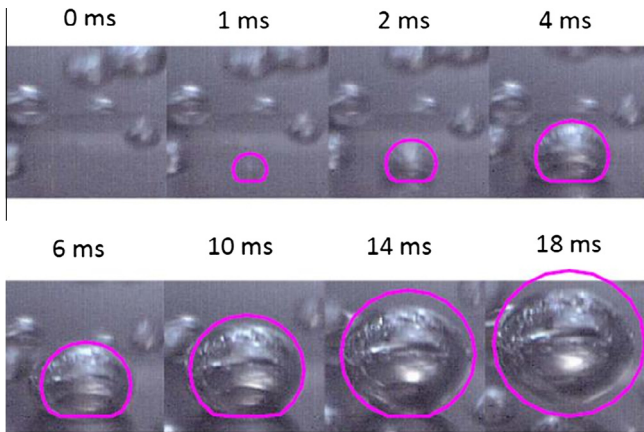
Fig. 19. Comparison of experimental [32] for a 25 μm thick titanium foil with applied heat flux of 50 kW/m² and simulation results for a bubble growing on a thin metal foil.

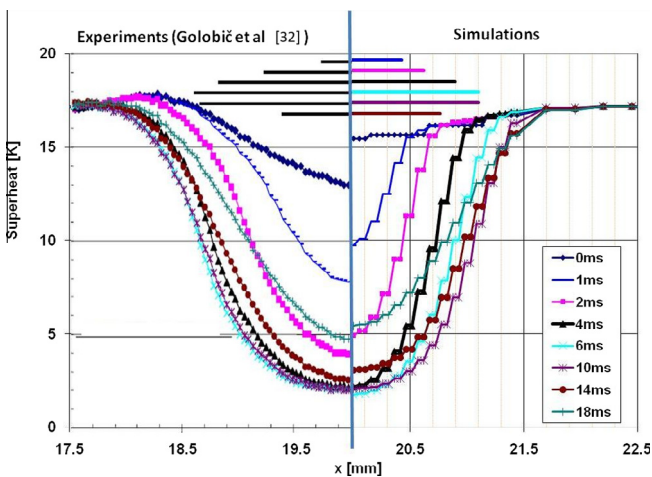**Fig. 21.** HTC distribution along a line passing through the nucleation site for titanium (25 μm). The diameter of the simulated contact area is also included.

Fig. 20. Superheat distribution along a line. Comparison of experiments and simulations for titanium (25 μm). The diameter of the simulated contact area is also included.

Fig. 22. Heat flux distribution along a line passing through the nucleation site for titanium (25 μm).

phenomena not included in the numerical model, do not appear in the numerical results. It must be also specified that the superheat distribution in experiments, was slightly asymmetrical with respect to the nucleation site (only half of the distribution is shown here). However, it was noted that for this range of variation the conditions outside the contact area do not significantly affect the bubble growth and superheat variation, mostly determined by the heat contributions, in particular at the dome. Similarly, Fig. 21 shows the comparison for the HTC distributions along a line passing through the nucleation site at different time steps. This shows a good agreement for the central HTC peak, apart for the case at $t = 4$ ms, when the experimental distribution appears much flatter than in the simulations. However, this phenomenon is probably related to the method used to derive the HTC distribution in [32], based on the variations of the temperature. Small errors in detection of this variable may lead to significantly greater differences in the HTC values. Finally, the comparison of the heat flux at the top surface along a line passing through the nucleation site is shown in Fig. 22. Three different trends can be distinguished. (1) During the initial stage, the heat flux has a central peak similar to the HTC distribution. (2) After that, for instance for $t = 2$ or 4 ms, the drop in superheat in the central area results in a drop in heat flux, so that the heat flux distribution assumes a crater like shape
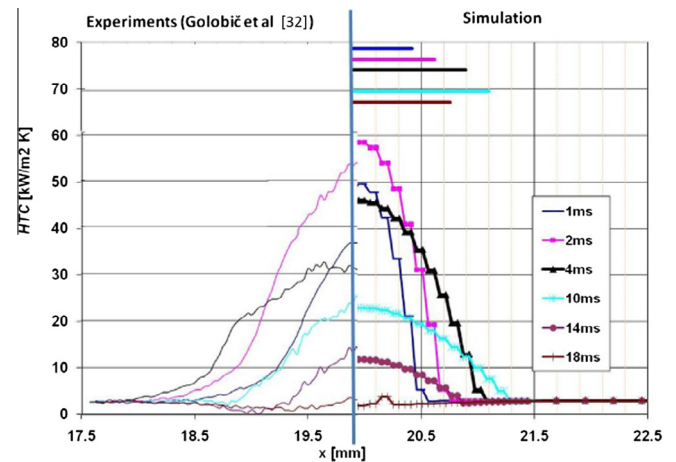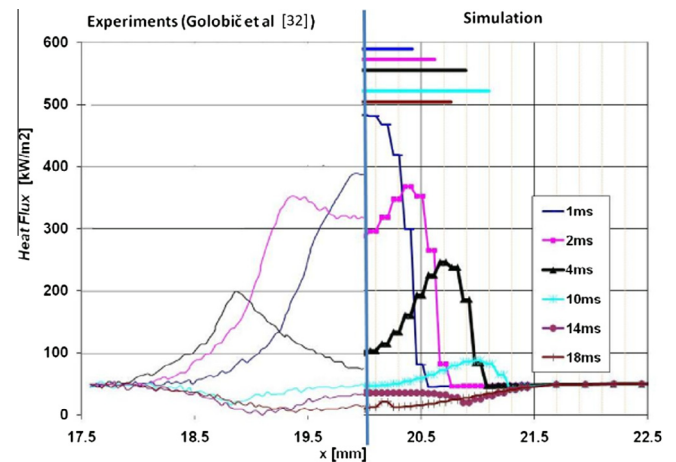
with a maximum in proximity of the contact area. During the final stage (3), the heat flux becomes smaller down to values similar to the natural convection area, leading also to a circular depression at the periphery of the contact area or immediately outside ($t \geqslant 10$ ms).

The analysis for the platinum foil with an imposed heat flux of 100 kW/m² was more complicated due to the lack of data provided in [35]. Only the contact and bubble radii when the bubble reached its maximum contact area and size were specified (respectively 0.775 and 1.1 mm). The analysis was made even more complicated by the lack of a visual sequence for the bubble growth due to other growing bubbles during the experiments. The bubble was said to depart 9 ms after nucleation. The superheat and HTC histories were extrapolated from the graphs along the line passing through the nucleation site, as listed in Table 4. Similar to the titanium case, the comparison between experiments and simulations for the bubble radius, superheat and HTC_{max} are shown in Fig. 23, highlighting a good agreement for superheat and HTC_{max}, apart for the intermediate stages ($t = 2$ and 3 ms) for the HTC_{max}.

For the bubble growth analysis, the uncertainty in the provided input data made the numerical results different from the experimental ones, although the final size was maintained. The difference during the initial stage is due to the quick increase of the bubble radius during the experiments that the code is not able to reproduce. Also, an important inconsistency between experimental

Table 4
Bubble growth data and superheat values at the nucleation site (Golobič et al. [35]). The data were obtained from graphs in the papers and are hence subject to a degree of uncertainty.

t [ms]	0	1	2	3	5	7	9
r_b [mm]	0		1.1				1.1
r_c [mm]	0		0.775				0
ΔT_{NS} [K]	16	2	2	2	2	4	7
HTC_{max} [kW/m^2]	8	105	55	55	50	22	8
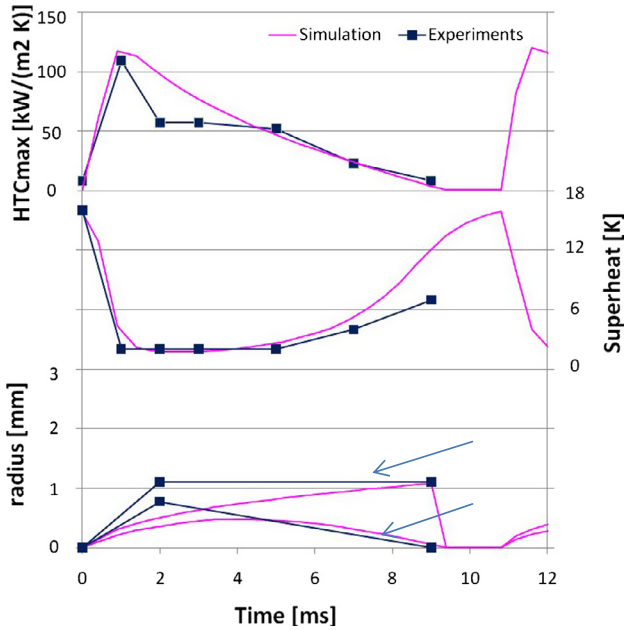
Fig. 23. Comparison between experimental [35] and simulation results for bubble and contact radii, superheat and HTC_{max} for platinum (6 μm).

Fig. 24. Superheat distribution along a line. Comparison of experiments and simulations for platinum (6 μm).

Fig. 25. HTC distribution along a line passing through the nucleation site for platinum (6 μm).

Fig. 26. Heat flux distribution along a line passing through the nucleation site for platinum (6 μm).

and numerical results is the waiting time, approximately equal to 40 ms for experiments and much shorter (~2 ms) for the simulations. This highlights that the activation model (that is simply based on the activation temperature) and the heat transfer mechanisms after bubble departure used in the code should be improved. This effect is probably due to the fact that the hydrodynamic phenomena in the liquid side are not taken into account by the code.
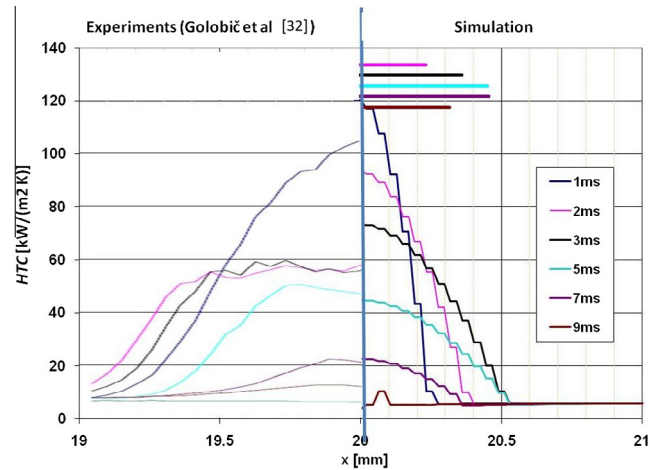
Figs. 24–26 show respectively the comparison of superheat, HTC and heat transfer along a diametrical line, highlighting that the influence area in the experiments is considerably larger than for simulations. In fact, the flat distributions visible even at 0.5 mm from the nucleation site in experiments (for $t = 2$ and 3 ms) are reduced to less than 0.2 mm in simulations. The agreement is generally good, but poorer than for the titanium case, which can possibly be related to the faster bubble growth (leading to a more complicated data acquisition) for platinum. In particular, for the heat transfer distribution, the crater shape simulated does not agree with experiments that show a central high peak. Also, it can be noted here that for $t = 2$, 3 and in part for 5 ms, the HTC distributions are flat and almost constant in the central area, highlighting a phenomenon only slightly visible for titanium at $t = 4$ ms.

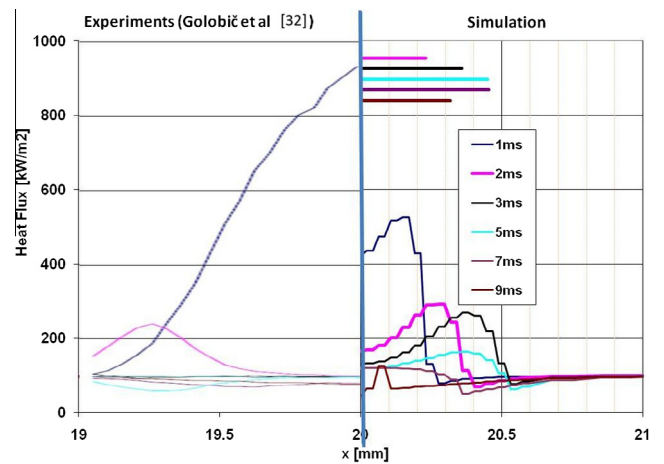## 6. Interactions between a large number of nucleation sites

The effects of interactions between a large number of potential nucleation sites, such as the variation of the local superheat, the activity of each nucleation site, the inhibition effects and the waiting time are presented in this section. Two different combinations of liquid and substrate are analysed, as it was during the single bubble growth analysis: a relatively thick silicon substrate

immersed in FC-72 and a very thin titanium foil in water. The concept of *unrefined sites* was also introduced here to take into account the boundary effects. The unrefined sites are located in the simulations in the areas close to the boundaries; for them, the mesh distribution is not modified during calculations and a simplified heat transfer model was used. This allows the simulation of a realistic heat transfer coefficient at the boundaries without further limit the number of nucleation sites and without loss in computational speed. The so-called *refined sites* (i.e. those using the mesh modification and heat transfer models, as described in the single bubble section) are located in the central area of the simulated substrate. For both analyses of silicon and titanium substrates, 100 refined sites were simulated. These sites are distributed in a regular square arrangement and the effect of the distance between them was analysed. Figs. 27 and 28 show the sites arrangements for the two cases. The sites are grouped in 6 different zones and identified with a numbers. For each substrate, the nominal parameters obtained from the single bubble analysis were used. Their values are summarised respectively in Tables 5 and 6. A second analysis was realised for the case of silicon in FC-72: this analysis takes into account an uncertainty on the nominal values of bubble departure radius and activation superheat. This means that for each of these two parameters, for each nucleation site and each time that this becomes active (except for the first activation) a random value is automatically and independently chosen by the code for the parameter, in a range ±10% of the nominal value. The value was chosen from the analysis of experimental results presented by Hutter et al. [31]. Simulations were run for 10 s.

6.1. Silicon substrate in FC-72

For the analysis of the silicon substrate in FC-72, the results for the bubble radius and for the superheat for 4 selected nucleation sites (#1, #32, #79 and #100) are shown in Fig. 29 for the case without uncertainty parameters (on the left side) and with the uncertainty parameter (on the right side). The figure clearly show that the superheat on average decreases in order to reach its asymptotic value during an initial transient period of ∼0.1s. During the second phase, called quasi-steady state, the superheat fluctuates around its mean value. The bubble distribution at the different nucleation sites is shown in Fig. 30 for all the active refined sites at different time steps for the case with the uncertainty parameter
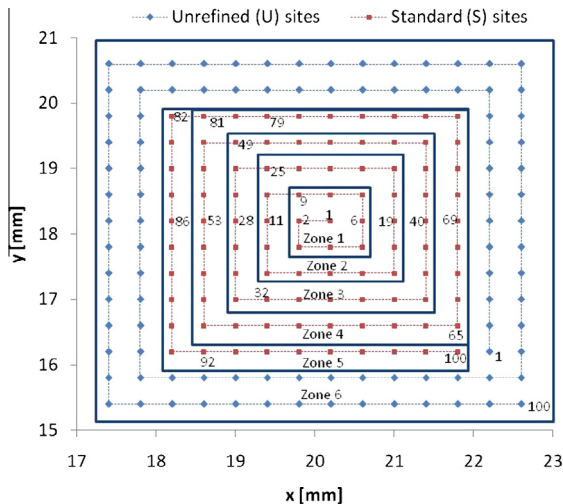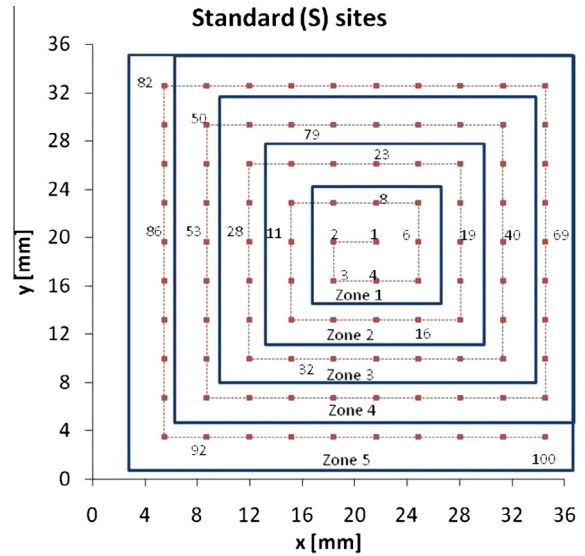

Fig. 28. Site distribution for titanium immersed in water with distance between sites 3.23 mm.

equal to 10%. The circles represent the computed bubble diameter. It is evident that while for the case (a) at $t = 0.1$ s the bubbles are growing similarly to the previous simulations with no uncertainty parameters, for the other cases, $t = 0.2$ (b), 2.1 (c) and 9.9 s (d), the bubble distribution becomes irregular with the bubbles growing out of phase. In fact, at $t = 0.2$ s the first effects of breaking the symmetry is visible in the central region, although in the external region the bubbles are still growing almost regularly. Instead, at $t = 5.3$ and 9.9 s, the loss of regularity is complete: big bubbles (also larger than the nominal bubble departure radius) are generally surrounded by much smaller bubbles or by areas where bubbles do not grow at all. The sites activities considering all the bubbles and the bubbles with large diameters (i.e. those having a departure radius larger than 0.1 times the nominal bubble departure radius) are shown in Fig. 31.
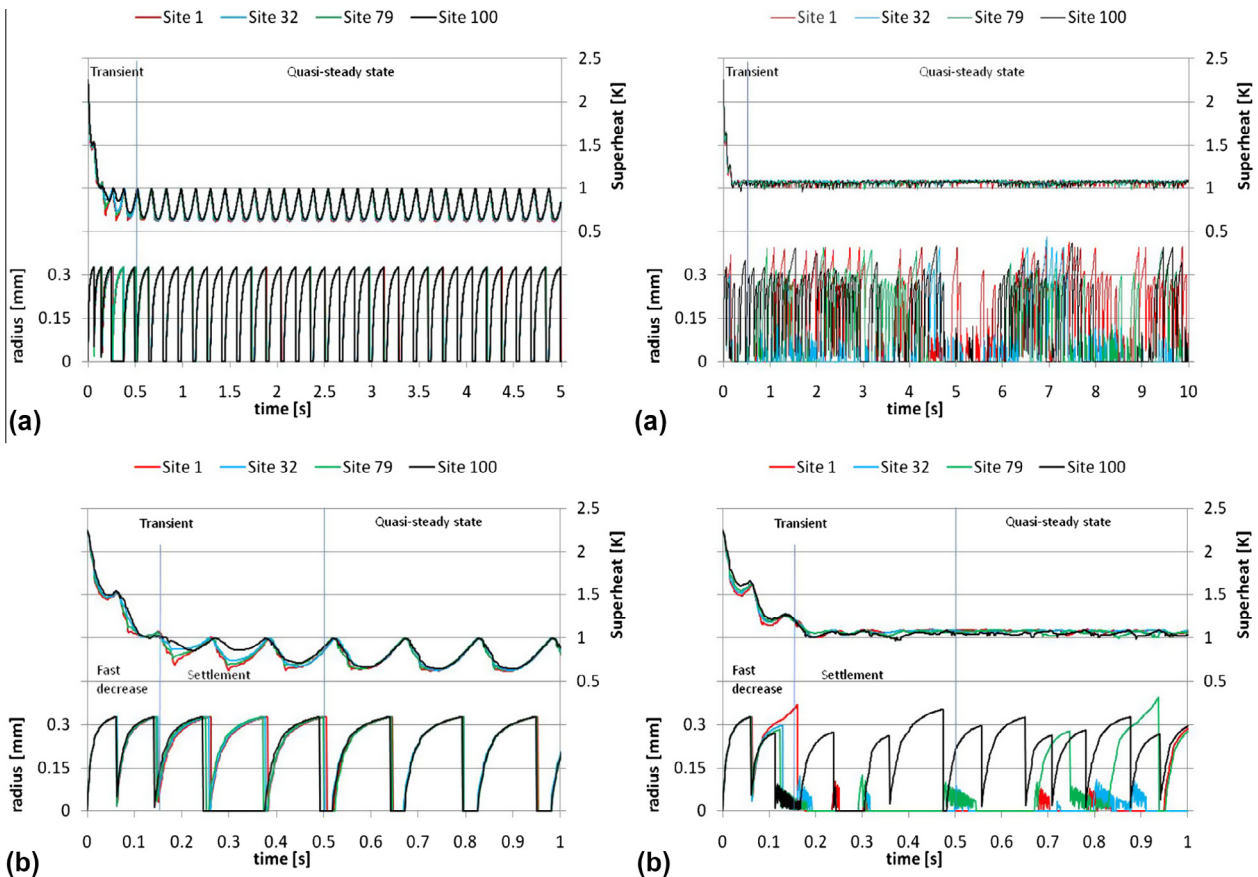
The growth time, the waiting time and the period for the two cases without and with uncertainty parameters are shown in Fig. 32. It is clear that, if for the case without uncertainty parameters, each bubble grows regularly and independently of the others, on the other case, the uncertainty parameters introduce almost immediately a perturbing factor that strongly reduces the superheat variations and the sites activity, such that the sites became immediately asynchronous. The growth times and the waiting times, quite regular for the case without uncertainty parameters, become very spread for the other case, although a clear tendency of increase with the calculation time is shown for the waiting time and the period. The effects of coalescence were also studied. Horizontal coalescence type C1 (bubbles of similar dimensions) was observed in both cases with and without uncertainty parameter. Coalescence occurrence was very regular for the case without uncertainty parameter and becomes more random for the other case. Fig. 33(a) shows a graphical representation of horizontal coalescence for the case with uncertainty parameter, the length of the blue lines proportional to the occurrence of coalescence type C1 between the connected sites. The phenomenon appears to be more frequent for the central sites and with the bubbles that are not immediately adjacent in the square arrangement. Fig. 33(b) shows coalescence type C2 (bubbles of different sizes, where the larger incorporates the smaller one): occurrence is more regular apart from the site close by the boundaries. This type of coalescence occurs more frequently between bubbles which are close spaced

Fig. 27. Site distribution for Silicon immersed in FC-72 with distance between sites 0.4 mm.

Table 5
Input data for a large distribution of sites for Silicon.

Substrate		δ_H	ρ_H	c_H	k_H	$\dot{q}$= 4.48 $\frac{kW}{m^2}$
[Silicon] 6.0 × 6.0 mm²		0.38 mm	2340 $\frac{kg}{m^3}$	750 $\frac{J}{kgK}$	110 $\frac{W}{mK}$	
Liquid [FC-72] 1 Atm, 57.15 °C		ρ_v	ρ_L	c_L	k_L 0.054 $\frac{W}{mK}$	H_{fg}
		12.76 $\frac{kg}{m^3}$	1611 $\frac{kg}{m^3}$	1088 $\frac{J}{kg\,K}$		85,200 $\frac{J}{kg}$
Bubble growth and heat Transfer	Exper	t_g	r_{bd}	ΔT_{act}	f_{decr}	ΔT_{IN}
		21.0 ms	0.33 mm	1 K	0.6	2.25 K
	Numer	HT model	HTC_{cl}	f_D	φ_0	Natural convection
		CL	~170 $\frac{kW}{m^2}$	1.0	30°	Eq. (3.15), f_{enh} = 1.16
Numerical data		Δt	w_{xy}	n_{vL}	n_R	Number of sites
		1.0 μs	0.1 mm	2	7	100 standard
						96 unrefined

Table 6
Input data for a large distribution of sites for titanium in water.

Substrate [Titanium] 36 × 36 mm²		δ_H 25 μm	ρ_H	c_H	k_H	$\dot{q}$= 50 $\frac{kW}{m^2}$
			4500 $\frac{kg}{m^3}$	523 $\frac{J}{kg\,K}$	21.9 $\frac{W}{m\,K}$	
Liquid [Water] 1 Atm, 100 °C		ρ_v	ρ_L	c_L	k_L	H_{fg}
		0.5974 $\frac{kg}{m^3}$	958 $\frac{kg}{m^3}$	4216 $\frac{J}{kg\,K}$	0.677 $\frac{W}{m\,K}$	2257300 $\frac{J}{kg}$
Single bubble growth and heat Transfer	Exper	t_g	r_{bd}	ΔT_{act}	f_{decr}	ΔT_{IN}
		18.1 ms	2.665 mm	15.5 K	0.6	17.5 K
	Numer	HT model	HTC_{maz}	f_D	φ_0	Natural convection
		ML	~80 $\frac{kW}{m^2}$	1.84	30°	Eq.(3.7), f_{enh} = 1.42
Numerical data		Δt	w_{xy}	n_{vL}	n_R	Number of sites
		0.5 μs	0.5 mm	2	7	100 standard

Fig. 29. Superheat variation at the nucleation site and bubble growth histories for the nucleation sites #1, #32, #79 and #100, for the nominal values on the left and for an uncertainties parameter equal to 10% on the right.

in the square arrangement. Fig. 34 shows the bubble growths at site #1 and at four surrounding sites immediately adjacent (#2, #4, #6 and #8), together with the superheat variations at the nucleation site #1 for the time period between 1.5 and 2 s of
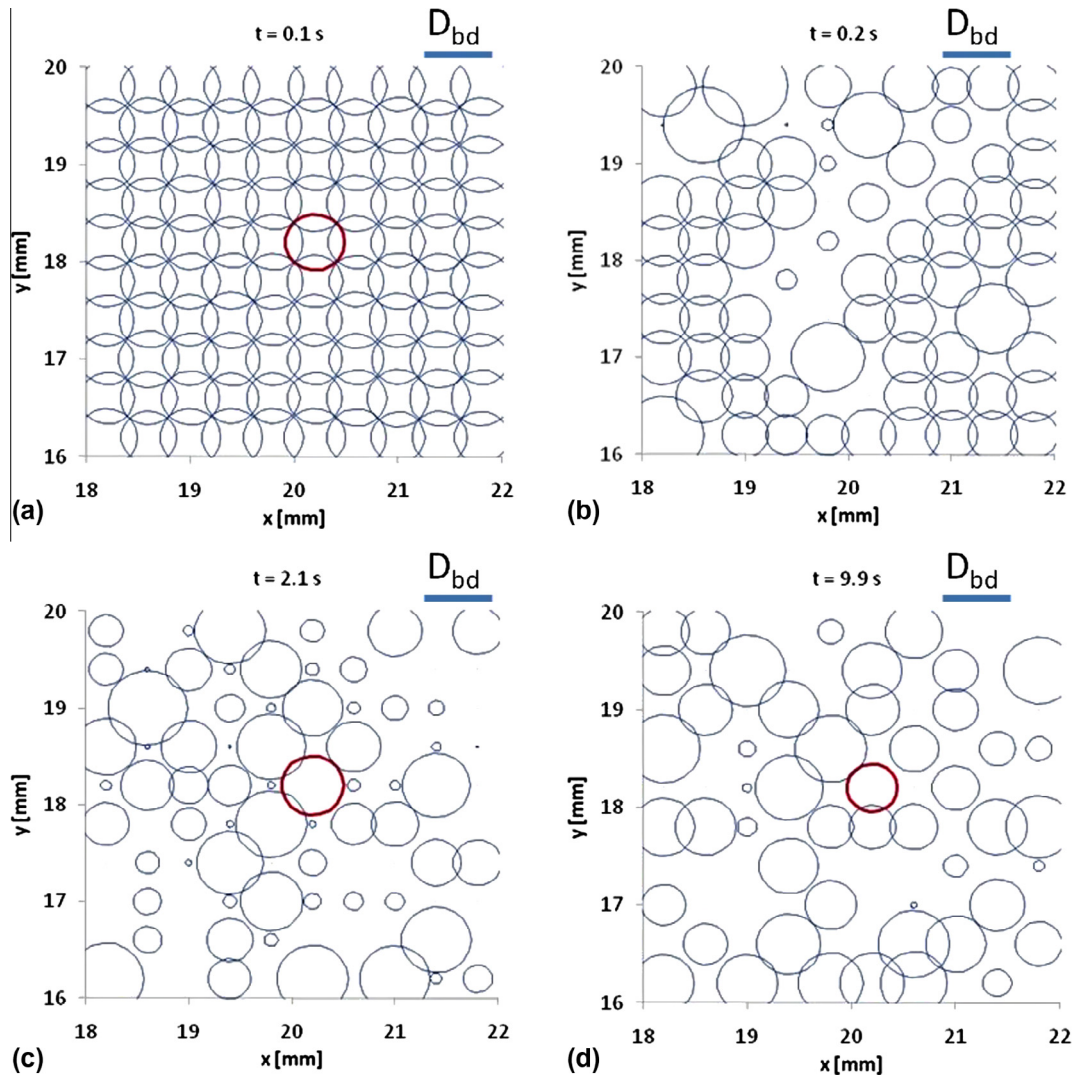
Fig. 30. Bubble distribution at the standard sites at different time steps when the uncertainty parameters are equal to 10% for the silicon substrate in FC72.
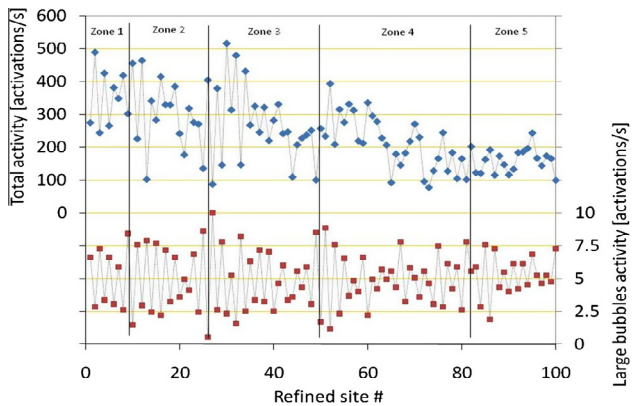

Fig. 31. Average activity of the nucleation sites during the quasi-steady state when using the uncertainty parameters equal to 10%. (a) Total activity. (b) Large bubble activity.

simulations. Four different phenomena are visible, indicated with an arrow and identified with the letters A, B, C and D. For the event A (1.585 s < t < 1.65 s) four time steps are identified (numbered from 1 to 4). The bubble growths and the superheat variations along the line connecting sites #2, #1 and #6 are shown in

Fig. 35 at the time steps corresponding to event A. For all the cases, the superheat variations at the base are very small (less than 0.1 K) and site #2 never becomes active. At $t = 1.585$ s (event A1), the bubbles at sites #1 and #6 have similar radii (the one at site #1 is slightly larger) and due to the close distance, the two domes interfere so that coalescence type C1 occurs. However, since the bubble radii for the bubble at site #1 is close to the departure radius, the contact angle and contact area are very small, so that the superheat variations are small as well. When the bubble at site #1 departs at $t = 1.59$ s, a new bubble starts growing, and at $t = 1.608$ s (Event A2), bubble at site #1 is through coalescence into bubble at site #6 (type C2, since $r_{b2} < 0.5\ r_{b6}$). This event forces the bubble at site #1 to disappear (after which a new small bubble is generated here at $t = 1.609$ s, Event A3) and the bubble at site #6 to undergo an increase of the bubble radius and bubble growth rate (Fig. 34), as well as an increase of the bubble departure radius. The bubble departure radius is further increased by sequential coalescence events type C2, not only of bubbles generated at site #1. During the two events A2 and A3 the superheat variation at site #6 does not change significantly, while at site #1 the variation is larger due to the sudden change in the size of the contact area. At $t \sim 1.649$ s, site #1 becomes completely inactive, due to the interference of the refined mesh with the ones of the surrounding sites.
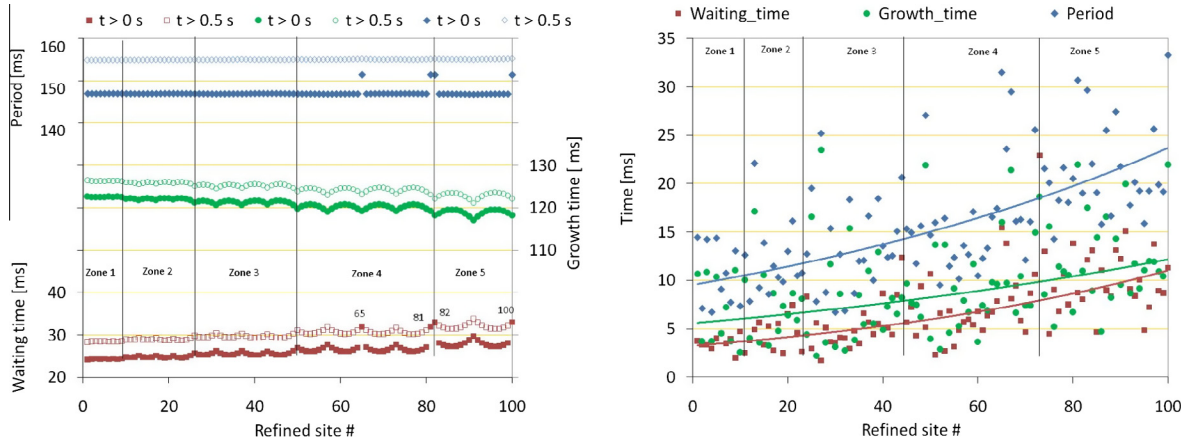
Fig. 32. Waiting time, growth time and period for the refined sites, for the nominal values on the left and for an uncertainties parameter equal to 10% on the right for the silicon substrate in FC72.
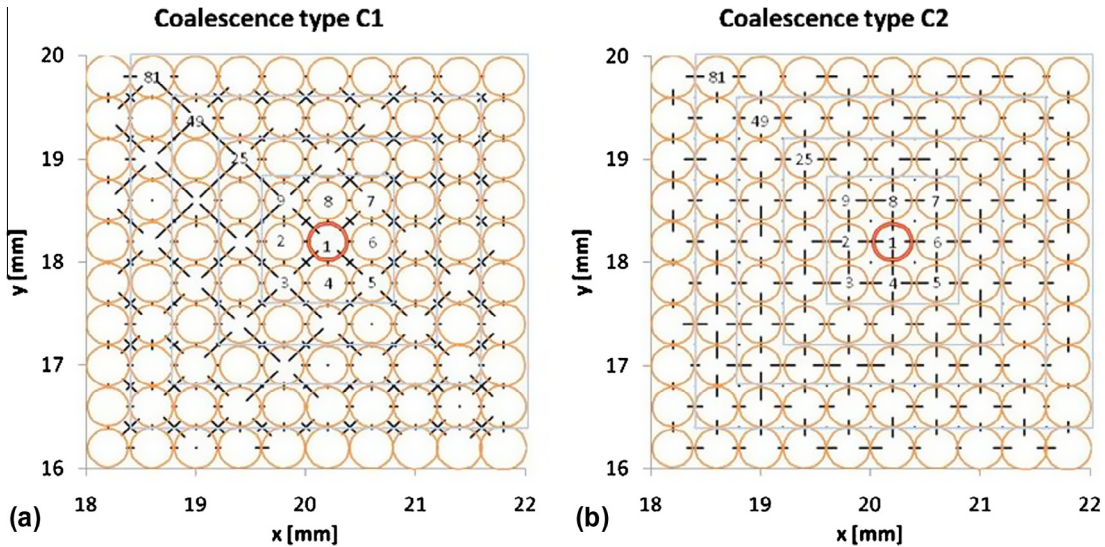

Fig. 33. Occurrence of coalescence type C1 (a) and C2 (b) for the silicon substrate in water for the case with uncertainty parameter for the silicon substrate in FC72.
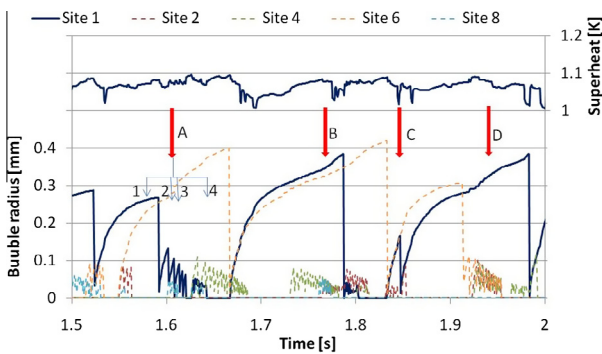

Fig. 34. Bubble growth histories and superheat variations at site #1 and the surrounding adjacent sites (#2, #4, #6, #8) for the silicon substrate in FC72.

At t = 1.65 s, site #1 is inactive and the superheat in that region further increased.

Event B is essentially similar to event A2, with bubbles at sites #1 and #6 having both large bubble radii and coalescing (type C1). However, in this case, both bubbles at sites #1 and #6 have incorporated bubbles from adjacent sites following coalescence type C2,

as evident from analysis of the bubble growth rate and the production of small bubbles at the other sites. Event C represents instead the case in which site #1 is forced to become inactive because of the limitations in the mesh distribution. This conclusion is derived by the absence in variation in bubble growth rate or bubble radius for the bubble at site #6 and confirmed by analysis of the coalescence event data.

Event D represents the opposite case with respect to event A2, with bubble at site #1 incorporating bubble at sites #6, #2, and #4.

6.2. Titanium foil in water

Concerning the analysis of the platinum foil immersed in water, the superheat variations at the nucleation site and the bubble growth histories for four different sites belonging to different zones (site #1, #32, #79 and #100) are shown for the initial stage (i.e. t < 0.75 s) and for the final stage (9.75 s < t < 10 s) respectively in Fig. 36(a) and (b). The transient period seems negligible in this case with respect to the case of silicon in FC-72, with the superheat at the nucleation site immediately fluctuating between ∼1.9 and 15.5 K. In the followings, the average values will be considered only for events occurring after the initial 0.5 s. Moreover, it is clear
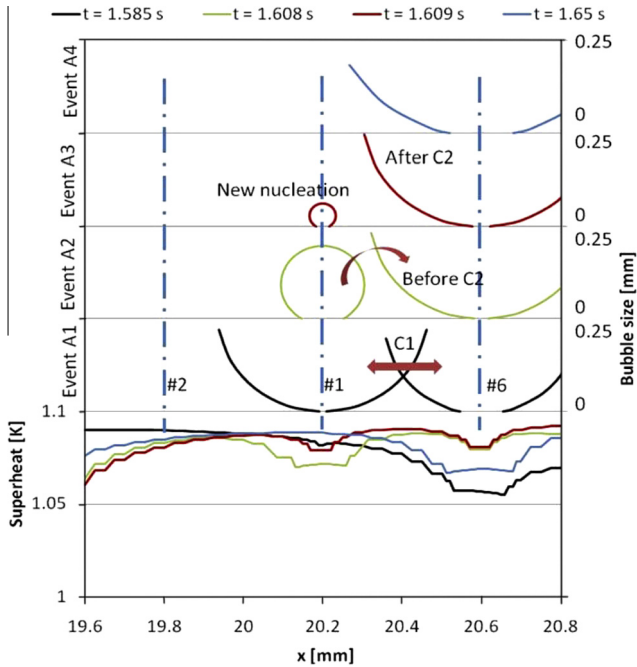
Fig. 35. Bubble growth and superheat distribution along the line passing through the nucleation sites #2, #1 and #6 for the silicon substrate in FC72.
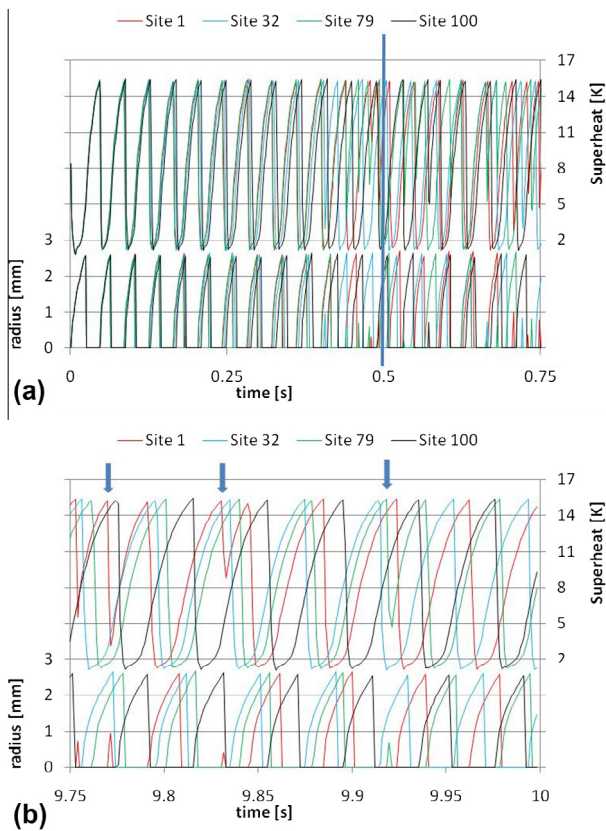
Fig. 36. Superheat variation at the nucleation site and bubble growth histories for the nucleation sites #1, #32, #79 and #100 on titanium. Uncertainty parameters = 0%.

that synchronization in bubble growth is lost after the short initial transient time, due to the large variations in superheat during the bubble growth that lead to an average superheat at departure

always lower than the activation value (15.5 K). Significant waiting times during which the superheat recovers can be consequently observed. For this reason, although the sites were arranged regularly and no uncertainty parameter was considered, the bubbles seem to grow independently from each other contrary to what was detected for the silicon substrate. The bubble distribution at different time steps shown in the presence of bubbles departing with small radii (indicated with the arrows in Fig. 36(b) at $t \sim 9.77$ and ~ 9.83 s for site #1 and at $t \sim 9.92$ s for site #79) highlights that coalescence phenomena are taking place. This highlights that thermal interactions across the substrate are much smaller for titanium due to the smaller thickness and lower thermal capacity. For this reason, the case with uncertainty parameter will be not examined. The bubble distribution at the different nucleation sites is shown in Fig. 37 for all the active standard sites at different time steps ($t = 0.25$ (a), 0.55 (b), 0.65 (c) and 9.5 s (d)). The lost in synchronization is visible already at $t = 0.25$ s (a). Here, most of the sites are active, but the radii slightly differ and some of them are inactive, with clear left–right symmetry in activation. The symmetry effect becomes more evident when the sites start to activate more independently, as it occurs in the central and lower part of the substrate for $t = 0.55$ and 0.65 s (cases (b) and (c)). However, this phenomenon is visible only until $t \sim 0.7$ s. The symmetry itself and the apparent larger activity in the lower part of the substrate during the first stage of simulations may have been generated by a chaotic behaviour of the system. Moreover, it seems that the sites activate in clusters defined for the purposes of this analysis as "groups of close sites with similar bubble growth characteristics", which assume particular geometries, for the entire length of simulations and an example of it is indicated by green arrows for $t = 9.5$ s (case (d)). A complete analysis of the presence of chaotic behaviour and activation in clusters is beyond the goal of this study. The sites activities considering all the bubbles and only the large bubbles (i.e. those having a departure radius larger than 0.1 times the nominal bubble departure radius) are shown in Fig. 38. This figure confirms that the sites act independently from each other. The growth time, the waiting time and the period are shown in Fig. 39. Bubbles seem to grow regularly and independently of the others, such that the sites became immediately asynchronous.

The analysis of occurrence of horizontal coalescence shows that both coalescence types C1 and C2 occur almost uniformly across the entire surface, but while type C1 involves all the eight sites surrounding a specific one (apart for those located close to the edges of the site distribution), type C2 involves only the four closest sites, since the distance between the others is too large to allow this type of coalescence. Examples of occurrence of coalescence types C1 are shown in Fig. 40, events A and B: in case A, after departure of a small bubble at site #1 due to coalescence, the site requires ~ 17 ms to become active again, while for event B the required time is ~ 11 ms. The difference depends on the size of the small departed bubble and on the superheat drop at the nucleation sites during its growth. At $t \sim 9.9$ s (event C) it is possible to observe the coalescence type C2, when site #1 incorporates the bubble at site #4, and undergoes a large increase of the bubble radius and of the bubble growth rate.

The analysis of coalescence occurrences showed that for type C2, the frequencies are much smaller, due to the absence of sequential coalescence (i.e. when a large bubble incorporates several small ones in a series) with respect to the silicon substrate. This phenomenon is connected to the waiting time: for silicon, the superheat was always higher or close to the activation value, while for titanium the site may require several milli-seconds before the conditions for activations are again satisfied.
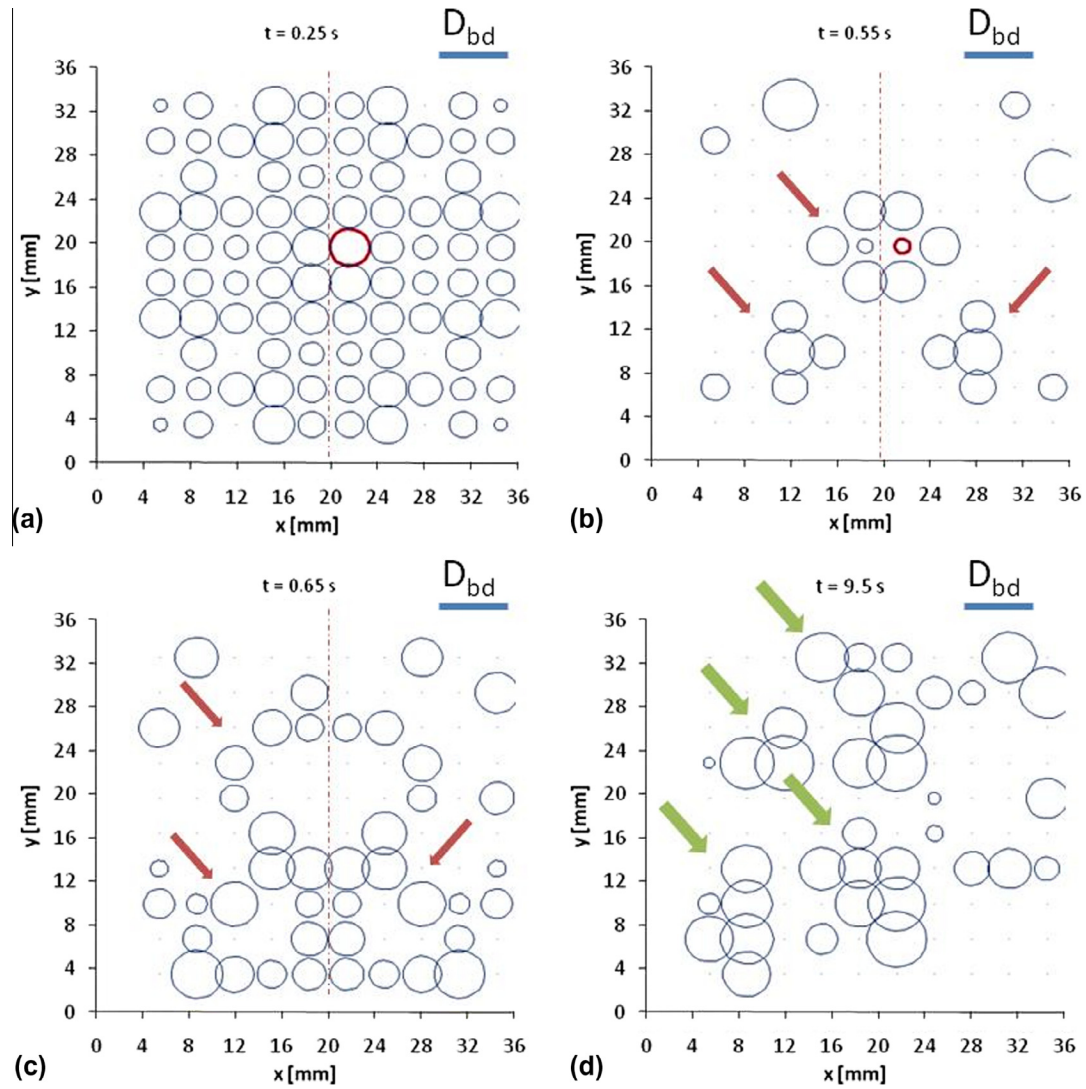
Fig. 37. Bubble distribution at the standard sites on titanium at different time steps when the uncertainty parameters are equal to 0.
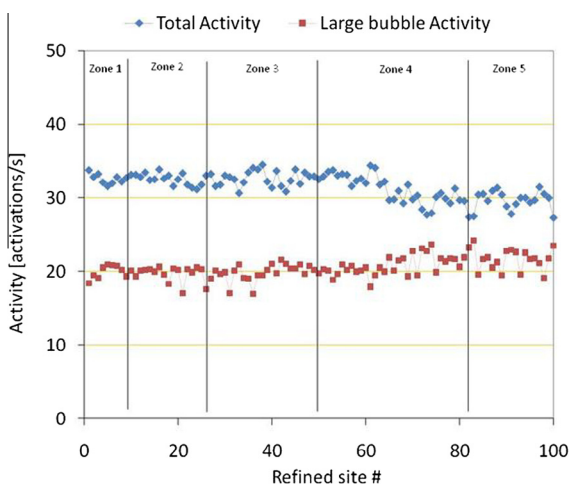

Fig. 38. Total activity of the nucleation sites depending on the nucleation site identification number.
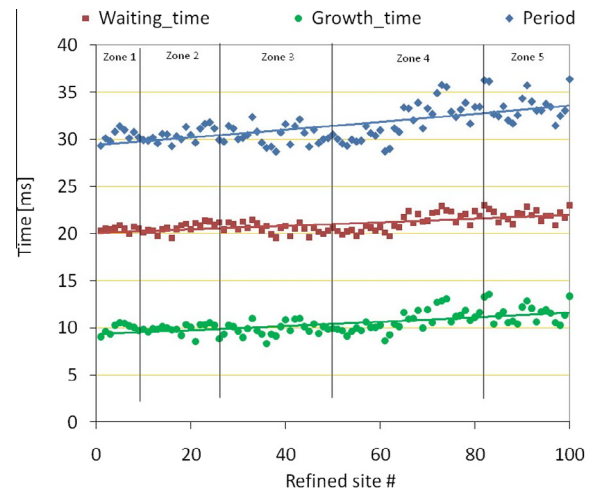

Fig. 39. Waiting time, growth time and period for the case with titanium and uncertainty parameters equal to 0.
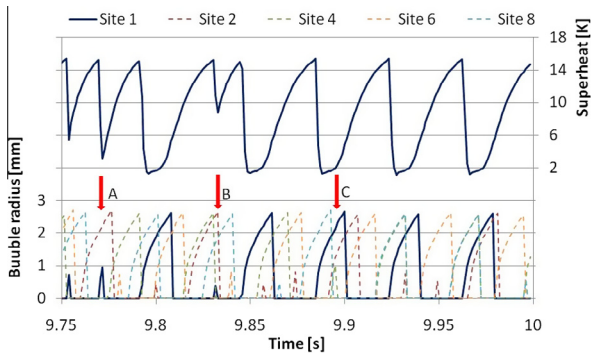
Fig. 40. Bubble growth histories involving coalescence and superheat variations at site #1 and the surrounding adjacent sites (#2, #4, #6, #8).

7. Conclusions

The numerical results obtained with this code, originally developed at the Los Alamos National Laboratory, have been compared with experimental results for silicon immersed in FC-72 and of metal foils, made of titanium and platinum, immersed in water at saturation conditions, so that they could be used in a first validation of the code mathematical models and processes. The two different models for the heat transfer at the base of the bubble were applied to the simulation for the silicon substrate in FC-72 and for the metal foil (titanium or platinum) in water, according to the experimental results. During the analysis for silicon in FC-72, the code was shown to be able to reproduce well the bubble growth at an isolated site with different applied heat fluxes. The experimental average superheat could be also predicted well, although the correlations used to evaluate the importance of the natural convection in the area outside the bubble contact area were tuned. However, analyses of long term superheat variations for an isolated nucleation site (presented in [31]), showed that the numerical code is able to reproduce well the transient superheat variations when the site switches from a period of regular activity to a period of inhibition and vice versa, although the physical reasons of this phenomenon was not fully understood. For this reason, the activity and inactivity periods have been imposed during the current simulations.

Validation of the code against results of bubble growing on thin metal foils showed that the code can reproduce very well the bubble growth and local superheat variations around the nucleation site (which was not isolated during these simulations), if the experimental heat flux conditions are imposed, and using the micro-layer heat transfer theory as a heat transfer model. The choice of the maximum heat transfer coefficients to be applied to the centre of the contact area was determined by the understanding of the very important and surprising similarity for the increasing–decreasing trend for the dimensionless heat transfer coefficient versus the dimensionless growth time for two essentially different cases of thin foils (titanium (25 μm) and platinum (7 μm)).

The capability of the code to adapt to different experimental conditions (i.e. variable input heat flux at the bottom of the substrate leading to different measured average superheat and bubble departure radii) was proved, although the heat transfer coefficients below the growing bubbles needed to be tuned to match the average bubble growth times.

The analysis of results for a distribution of 100 potential nucleation sites allowed the conclusion that the substrate-liquid combination strongly affects the variation of superheat and the relative influence area. It was shown that for titanium in water the superheat variation was very similar to the single bubble case. By contrast, for silicon on FC-72 the average superheat at the nucleation site dropped from ∼8 K for the single bubble case to ∼1 K (and then comparable to the activation superheat) for the large distribution.

Moreover, uncertainties in the input data and the possibility of occurrence of coalescence may play a very important role in the regularity of activation of the sites and the growth of the bubbles. In fact, the introduction of uncertainty parameters for the case of silicon substrate in FC-72 used to correct the nominal values introduced differences in the average activity of the sites. This suggests that this phenomenon cannot be neglected: further studies are required to refine the current modes of mesh refinement and coalescence, also according to experimental findings. Considering the case when the uncertainty parameters were used, the site activation frequency was not uniform for all the sites over the whole surface, showing a distribution with alternating more active sites.

The case of titanium on water, only developed without taking into account the uncertainty parameters, showed that the sites lost synchronisation in activation after only few activation cycles. Activation in clusters seemed to occur, although the final average activation frequency was similar for all the sites. Both type of coalescence occurred in this case, although for the type for dissimilar sizes the frequency was greatly smaller than for the case of silicon on FC-72.

Comparison of the results for a thick silicon substrate in FC72 and a thin titanium foil in water showed also that stronger thermal interaction between sites was recognisable for the silicon case, leading to lower average superheat around the nucleation sites for a large distribution of sites with respect to an isolated site. This led also to much larger growth times, due to the smaller heat flux contribution at the base of the bubble. Moreover, the superheat distribution across the substrate became flatter. On the contrary, for the titanium case all the sites appear to act more independently, and the superheat variations to be very similar between an isolated site and a large distribution.

From the numerical point of view, the capacity of the code in adapting its mesh distribution and the ease in modifying correlations and conditions according to the different situations simulated make it a very powerful instrument to investigate thermal interactions despite of the simplicity of some of the models, as for instance the one for horizontal coalescence.

Conflict of interest

None declared.

Acknowledgements

References

[1] W.M. Rohsenow, A method of correlating heat transfer data for surface boiling of liquids, J. Heat Transfer Trans. ASME 74 (1952) 969–976.
[2] K. Engelberg-Forster, R. Greif, Heat transfer to a boiling liquid – mechanism and correlations, J. Heat Transfer Trans. ASME 81 (1959) 43–53.
[3] H.K. Forster, N. Zuber, Dynamics of vapour bubbles and boiling heat transfer, AIChE J. 1 (4) (1955) 531–535.
[4] Y.Y. Hsu, On the size range of active nucleation cavities on a heating surface, J. Heat Transfer Trans. ASME 84 (1962) 207–216.
[5] C.Y. Han, P. Griffith, The mechanism of heat transfer in nucleate pool boiling – part I, Int. J. Heat Mass Transfer 8 (1965) 887–904.
[6] T.W. Forest, The stability of gaseous nuclei at liquid-solid interfaces, J. Appl. Phys. 53 (1982) 6191–6201.
[7] W. Tong, A. Bar-Cohen, T.W. Simon, S.M. You, Contact angle effects on boiling incipience of highly-wetting liquids, Int. J. Heat Mass Transfer 33 (1990) 91–103.

[8] D.B.R. Kenning, What do we really know about nucleate boiling? in: 6th UK National Heat Transfer Conference, Edinburgh, 1999, pp. 143–167.

[9] A.K. Chesters, Modes of bubble growth in the slow-formation regime of nucleate pool boiling, Int. J. Multiphase Flow 4 (1978) 279–302.

[10] M.S. Plesset, S.A. Zwick, The growth of vapor bubbles in superheated liquids, J. Appl. Phys. 25 (4) (1954) 493–500.

[11] H.K. Forster, N. Zuber, Growth of a vapour bubble in a superheated liquid, J. Appl. Phys. 25 (4) (1954) 474–478.

[12] B.B. Mikic, W.M. Rohsenow, P. Griffith, On bubble growth rates, Int. J. Heat Mass Transfer 13 (1970) 657–666.

[13] A. Prosperetti, M.S. Plesset, Vapour-bubble growth in a superheated liquid, J. Fluid Mech. 85 (2) (1978) 349–368.

[14] C.Y. Han, P. Griffith, The mechanism of heat transfer in nucleate pool boiling – part II, Int. J. Heat Mass Transfer 8 (1965) 905–913.

[15] B.B. Mikic, W.M. Rohsenow, A new correlation of pool-boiling data including the effect of heating surface characteristics, J. Heat Transfer Trans. ASME 91 (1969) 245–250.

[16] K. Stephan, M. Abdelsalam, Heat-transfer correlations for natural convection boiling, Int. J. Heat Mass Transfer 23 (1980) 73–87.

[17] I.L. Pioro, W. Rohsenow, S.S. Doerffer, Nucleate pool-boiling heat transfer. II: assessment of prediction methods, Int. J. Heat Mass Transfer 47 (2004) 5045–5057.

[18] G. Son, V.K. Dhir, N. Ramanujapu, Dynamics and heat transfer associated with a single bubble during nucleate boiling on a horizontal surface, J. Heat Transfer Trans. ASME 121 (1999) 623–631.

[19] G. Son, N. Ramanujapu, V.K. Dhir, Numerical simulation of bubble merger process on a single nucleation site during pool nucleate boiling, J. Heat Transfer Trans. ASME 124 (2002) 51–62.

[20] V.K. Dhir, Mechanistic prediction of nucleate boiling heat transfer – achievable or a hopeless task?, J Heat Transfer Trans. ASME 128 (2006) 1–12.

[21] D.B.R. Kenning, Wall temperature patterns in nucleate boiling, Int. J. Heat Mass Transfer 35 (1992) 73–86.

[22] D.B.R. Kenning, Y. Yan, Pool boiling heat transfer on a thin plate: features revealed by liquid crystal thermography, Int. J. Heat Mass Transfer 39 (1996) 3117–3137.

[23] M. Shoji, L. Zhang, S. Chaptun, Nucleation site interaction in pool nucleate boiling – serial experiments using artificial boiling surfaces, in: 6th World Conference on Experimental Heat Transfer, Fluid Mechanics, and Thermodynamics, Matsushima, Miyagi, April 2005.

[24] P. Stephan, J. Hammer, A new model for nucleate boiling heat transfer, Wärme Stoffübertrag. 30 (1994) 119–125.

[25] P. Stephan, T. Fuchs, E. Wagner, N. Schweizer, Transient local heat fluxes during the entire vapor bubble life time, in: ECI International Conference on Boiling Heat Transfer, Florianópolis, Brazil, 2009.

[26] L. Zhang, M. Shoji, Nucleation site interaction in pool boiling on an artificial surface, Int. J. Heat Mass Transfer 46 (2003) 513–522.

[27] A. Calka, R.L. Judd, Some aspects of the interaction among nucleation sites during saturated nucleate boiling, Int. J. Heat Mass Transfer 28 (1985) 2331–2342.

[28] K.O. Pasamehmetoglu, R.A. Nelson, Cavity to cavity interaction in nucleate boiling: the effect of heat conduction within the heater, AIChE J. 87 (1991) 342–351.

[29] I. Golobič, E. Pavlovič, S. Strgar, D.B.R. Kenning, Y. Yan, Wall temperature variations during bubble growth on a thin plate: computation and experiments, in: Eurotherm Seminar No. 48, 1996, pp. 25–32.

[30] I. Golobič, E. Pavlovič, J. Hardenberg, M. Berry, R.A. Nelson, D.B.R. Kenning, L.A. Smith, Comparison of a mechanistic model for nucleate boiling with experimental spatio-temporal data, Trans. IChemE 82 (2004) 435–444.

[31] C. Hutter, D.B.R. Kenning, K. Sefiane, T.G. Karayiannis, H. Lin, G. Cummins, A.J. Walton, Experimental pool boiling investigations of FC-72 on silicon with artificial cavities and integrated temperature microsensors, Exp. Therm. Fluid Sci. 34–4 (2010) 422–433.

[32] I. Golobič, M. Bašelj, A. Papez, J. Petkovsek, D.B.R. Kenning, Bubble coalescence in pool boiling on a thin foil investigated by high-speed IR thermography, in: 13th International Heat Transfer Conference, Sydney, Australia, 2006.

[33] 3M. 2006. Speciality materials, Fluorinert liquid FC-72, Product information.

[34] J.L. Parker, M.S. El-Genk, Enhanced saturation and subcooled boiling of FC-72 dielectric liquid, Int. J. Heat Mass Transfer 48 (2005) 3736–3752.

[35] I. Golobič, J. Petkovsek, M. Bašelj, A. Papez, D.B.R. Kenning, Experimental determination of transient wall temperature distributions close to growing vapor bubbles, Heat Mass Transfer 45 (2009) 857–866.

[36] P. Stephan, T. Fuchs, Local heat flow and temperature fluctuations in wall and fluid in nucleate boiling systems, in: ECI International Conference on Boiling Heat Transfer, Spoleto, Italy, 2006.

[37] D.B.R Kenning, I. Golobič, J. Petkovsek, Pool boiling: global correlations and mechanistic studies, in: UK National Heat Transfer Conference, London, UK, 2009.